Acta Biomaterialia 152 (2022) 273–289

Contents lists available at ScienceDirect

Acta Biomaterialia

journal homepage: www.elsevier.com/locate/actbio

Full length article

Role of stiffness and physico-chemical properties of tumour microenvironment on breast cancer cell stemness

Lekha Shah[a], Ayşe Latif[a], Kaye J. Williams[a], Annalisa Tirella[a,b,*]

[a] Division of Pharmacy and Optometry, Faculty of Biology, Medicine and Health, University of Manchester, Oxford Road, M13 9PL, Manchester, United Kingdom
[b] BIOtech - Center for Biomedical Technologies, Department of Industrial Engineering, University of Trento, Via delle Regole 101, Trento 38123, Italy

ARTICLE INFO

Article history:
Received 11 May 2022
Revised 29 August 2022
Accepted 30 August 2022
Available online 8 September 2022

Keywords:
Breast cancer stem cells
Tumour micro-environment
3D *in vitro* models
Stiffness
Tumour-on-a-chip

ABSTRACT

Several physico-chemical properties of the tumour microenvironment (TME) are dysregulated during tumour progression, such as tissue stiffness, extracellular pH and interstitial fluid flow. Traditional preclinical models, although useful to study biological processes, do not provide sufficient control over these physico-chemical properties, hence limiting the understanding of cause-effect relationships between the TME and cancer cells. Breast cancer stem cells (B-CSCs), a dynamic population within the tumour, are known to affect tumour progression, metastasis and therapeutic resistance. With their emerging importance in disease physiology, it is essential to study the interplay between above-mentioned TME physico-chemical variables and B-CSC marker expression. In this work, 3D *in vitro* models with controlled physico-chemical properties (hydrogel stiffness and composition, perfusion, pH) were used to mimic normal and tumour breast tissue to study changes in proliferation, morphology and B-CSC population in two separate breast cancer cell lines (MCF-7 and MDA-MB 231). Cells encapsulated in alginate-gelatin hydrogels varying in stiffness (2-10 kPa), density and adhesion ligand (gelatin) were perfused (500 µL/min) for up to 14 days. Physiological (pH 7.4) and tumorigenic (pH 6.5) media were used to mimic changes in extracellular pH within the TME. We found that both cell lines have distinct responses to changes in physico-chemical factors in terms of proliferation, cell aggregates size and morphology. Most importantly, stiff and dense hydrogels (10 kPa) and acidic pH (6.5) play a key role in B-CSCs dynamics, increasing both epithelial (E-CSCs) and mesenchymal cancer stem cell (M-CSCs) marker expression, supporting direct impact of the physico-chemical microenvironment on disease onset and progression.

Statement of significance

Currently no studies evaluate the impact of physico-chemical properties of the tumour microenvironment on breast cancer stem cell (B-CSC) marker expression in a single in vitro model and at the same time. In this study, 3D in vitro models with varying stiffness, extracellular pH and fluid flow are used to recapitulate the breast tumour microenvironment to evaluate for the first time their direct effect on multiple breast cancer phenotypes: cell proliferation, cell aggregate size and shape, and B-CSC markers. Results suggest these models could open new ways of monitoring disease phenotypes, from the early-onset to progression, as well as being used as testing platforms for effective identification of specific phenotypes in the presence of relevant tumour physico-chemical microenvironment.

1. Introduction

Remodelling of the extracellular matrix (ECM) by cancer cells affects tumour progression and metastasis [1]. Conversely, variation of ECM properties, such as matrix stiffness and composition, extracellular pH, and other physico-chemical properties have also been recognised to impact tumorigenesis and metastatic formation [2]. To better understand changes within the tumour microenvironment (TME), and how these contribute to tumour development, new and more comprehensive pre-clinical models are required. Breast cancer stem cells (B-CSCs) are a dynamic tumour initiating cell population within the tumour milieu, with a key role

* Corresponding author at: BIOTech Center for Biomedical technologies, University of Trento, Via delle Regole 101, Trento 38123, Italy.
E-mail address: annalisa.tirella@unitn.it (A. Tirella).

https://doi.org/10.1016/j.actbio.2022.08.074

in tumorigenesis, metastasis, recurrence and therapeutic resistance [3–6]. Recently, reports on interactions of CSCs and the TME are gaining traction but yet remain poorly understood [7,8]. In terms of B-CSCs characterisation, Al-Hajj et al. firstly reported that patient-derived B-CSCs showed a $CD44^{+}/CD24^{-/low}$ sub-population with high tumour initiating capacity and self-renewal. Additionally this subpopulation was able to rebuild the heterogeneity of the original tumour in immunocompromised mice [9]. CD44 is a transmembrane glycoprotein with its main ligand as hyaluronic acid. Roles for CD44 have been implicated in cell proliferation and increased cell survival [10]. Furthermore, CD44 is expressed in circulating tumour cells (CTCs) that have metastasis initiating capacity [11,12]. CD24 is a glycosylated membrane anchored protein mainly present on immune cells [13]. Later studies identified another marker, aldehyde dehydrogenase (ALDH), associated with stem progenitor cells, found in both normal breast as well as cancer tissue [14]. Co-localisation analysis of immunofluorescence stained breast cancer tissues reported that the $CD44^{+}/CD24^{-}$ B-CSC subpopulation is distinct from the $ALDH^{+}$ one, with minimal overlap among these two groups [15]. Similarly, comparison of gene expression showed mainly reciprocal patterns with either mesenchymal or epithelial characteristics. The $CD44^{+}/CD24^{-}$ subpopulation had enriched mesenchymal markers including vimentin, matrix metalloproteinase-9 (MMP-9) and Zinc finger E-box-binding homeobox-1 (ZEB1), and exhibited quiescent mesenchymal phenotype further termed as mesenchymal type-cancer stem cells (M-CSCs). In contrast, the $ALDH^{+}$ subpopulation had higher expression of epithelial associated markers including E-cadherin, claudins and occludins, which presented a proliferative epithelial phenotype, termed as epithelial type cancer stem cells (E-CSCs) [15]. These B-CSCs also show plasticity and transition between epithelial and mesenchymal states [15]. It remains important to understand if interactions with TME can affect B-CSCs and their plasticity. Physico-chemical properties of TME- matrix stiffness, density, matrix composition, pH and interstitial fluid flow are known to be dysregulated, affecting cancer risk, tumour progression and therapeutic efficiency [16,17]. Most solid tumours like breast cancer have increased stiffness than the adjoining normal tissue, as well as a state of fibrosis known as 'desmoplasia' [18]. Compression analysis of *ex vivo* breast cancer samples showed that average elastic modulus of normal breast tissue is approximately 3 kPa, whereas for DCIS (Ductal carcinoma in situ) it is 16 kPa, proving a three to six-fold increase in stiffness for malignant tumours [19]. Atomic force microscopy (AFM) analysis of breast tumours observed an average of four-fold increase for invasive lesions compared to normal tissue (normal tissue 0.4-1 kPa; invasive ductal carcinoma (IDC) 2-4 kPa). The same study correlated increase in stiffness and collagen deposition to breast cancer stage progression from DCIS to IDC (invasive ductal carcinoma) [20]. Another factor, acidic extracellular pH (further referred to as 'pH' only), is caused by increased aerobic glycolysis in the TME that lowers the pH values in the range of 6.5-6.9 when compared to normal tissue pH (typically reported in the range of 7.2-7.5) [21,22]. In addition, decrease of pH has been linked to tumour aggressiveness [23], angiogenesis [24], and disruption of the cellular circadian clock [25]. Another important factor on mechanical forces transmission within the TME is the interstitial fluid flow and the perfusion of fluids through the ECM, with a proven effect on tissue morphogenesis, pathogenesis as well as cell mechanobiology [26,27]. The heterogeneous nature of such mechanical forces makes it difficult to determine exact values (and/or variations) in each microenvironment *in vivo* [28]. Mathematical models and experimental data estimate a rather wide range of interstitial fluid flow values in normal and tumour tissues (0.1-10 μm/s), sharing a common conclusion that higher flow velocities are present at the tumour edge when compared to the tumour core [27]. Advanced *in vitro* models, also known as tumour-on-a-chip, intended to mimic the *in vivo* perfusion with values ranging from 0.2 μm/s [29] to 10 μm/s [30] have been intensively used to study effects of fluid flow on cellular polarisation, proliferation, and migration. Of note, these studies suggest that increased cell migration speed and invasion is observed in three-dimensional (3D) hydrogels in perfused (or dynamic) culture conditions when compared to static traditional culture (i.e. without interstitial flow). While these physico-chemical cues have been independently investigated, their combined role in breast cancer phenotypes and B-CSCs have not yet been deciphered due to the lack of appropriate models. What we now know is that traditional models lack physiological complexity, whereas animal models provide insufficient control over these TME properties [31]. To overcome this insufficient control associated with the use of animal models and to precisely study effects of the interplay between the TME and B-CSCs, new approaches are required to model the physico-chemical cues of TME in 3D by controlling material composition and stiffness, pH, and/or interstitial flow [32]. This study describes precision 3D *in vitro* models designed to mimic variations of breast tissue homeostasis, and its use to understand the cause-effect relationship between TME physico-chemical cues and breast cancer phenotypes. A small library of hydrogels (alginate-gelatin) with known matrix compressive elastic moduli, varying from normal breast tissue (~2 kPa, soft) to malignant breast tissue (~10 kPa, stiff) [19] was used to encapsulate two breast cancer cell lines: luminal and lower grade cell line MCF-7, and higher grade triple negative (TNBC) cell line MDA-MB-231. As alginate lacks in cell-adhesive domains, gelatin was included in hydrogel formulations to promote cell-matrix interactions and to mimic increased collagen deposition and tissue density, as observed in breast tumours. Variations of interstitial fluid flow and tissue perfusion were controlled using the Quasi Vivo milli-fluidic system (500 μL/min); whereas different media composition was used to model pH variations (i.e. 6.5 and 7.4). Effect of TME variables was evaluated on cell proliferation, morphology and B-CSCs markers (CD44, CD24, Vimentin, E-cadherin and ALDH). Our findings suggests that TME affects cellular heterogeneity and B-CSCs plasticity, which could further direct tumour progression and metastases at distant sites [4,33]. This work describes the next generation of non-animal technologies: 3D *in vitro* models allowed independent control of TME variables on B-CSCs, allowing for the first time to gain insight in their role on breast tumour progression and suggesting their use to better predict disease phenotypes.

2. Materials and methods

2.1. Alginate-gelatin hydrogel preparation

HEPES buffered saline (HBS) was prepared by dissolving 20 mM HEPES (H4034, Sigma Aldrich UK) and 150 mM NaCl in distilled water. High-mannuronic sodium alginate (G/M ratio of 0.7, Pro-Alg, Chile) powder was reconstituted in HBS at concentrations of 3% and 6% (w/v) overnight on a shaker at room temperature (RT). Alginate solutions (aq.) were sterile filtered using a 0.22 μm polyethersulfone (PES) filter (SLGP033RS, MERCK) prior to cell culture use. Similarly, gelatin type A (G1890, Sigma-Aldrich, UK) was hydrated (2 h, 37°C) in HBS at concentrations of 2% and 6% (w/v); and further sterile filtered with a 0.45 μm polyvinylidene-difluoride (PVDF) filter (SLHV033RS, MERCK) prior to use. Alginate-gelatin solutions were prepared by mixing different concentrations of alginate and gelatin solutions in 1:1 volume ratio (5 min, RT) as listed in Table 1.

Calcium chloride ($CaCl_2$, C/1400/53, Fischer scientific, UK) solutions were prepared in distilled water at concentrations of 100 mM, 200 mM and 300 mM. Each solution was sterile filtered prior

Table 1
Alginate-based hydrogels: composition and physical properties. Hydrogels were crosslinked with $CaCl_2$ (aq.) at concentrations of 100 mM, 200 mM and 300 mM (RT, 10 min). In table, protein content (i.e. gelatin concentration) and density (i.e. polymers concentration) are classified as high, medium and low.

Alginate concentration % (w/v)	Gelatin concentration % (w/v)	Protein content	Density % (w/v)		Sample ID
1.5	1	Low	2.5	Low	A1.5G1
1.5	2	Medium	3.5	Low	A1.5G2
1.5	3	High	4.5	Medium	A1.5G3
3	1	Low	4	Medium	A3G1
3	2	Medium	5	High	A3G2
3	3	High	6	High	A3G3

use (0.22 µm PES filter) and stored at 4°C until use. A small library of hydrogels was obtained by crosslinking alginate-gelatin solutions with $CaCl_2$ (aq.) (Table).

2.2. Unconfined compression tests: hydrogel stiffness

Compressive elastic moduli (from now on referred to as stiffness for simplicity) of hydrogels were determined by uniaxial compressive tests using the Texture Analyzer (TA.XT plus, Stable microsystems) equipped with 5N load cell. Compressive tests were performed using a zero-stress initial condition (i.e. configuration with no contact between the sample and the probe) [34]. Briefly, cylindrically shaped hydrogels (Section SI 1.5) were compressed with a constant speed (0.05 mm/sec). A stress-strain plot was obtained for each samples, and the slope within the 0.05 strain interval was used to calculate the stiffness (kPa) of each hydrogels (Section SI 1.6) [34,35]. All measurements were performed using at least n=4 samples for each group and two independent experiments. All data are represented as mean ± standard deviation (st.dev.).

2.3. Cell culture

2.3.1. Cell lines

Human breast adenocarcinoma cell lines MCF7 and MDA-MB-231 were selected for this study. Prior use, both cell lines were authenticated by European Collection of Authenticated Cell Cultures (ECACC, operated by Public Health England). Cells were routinely cultured in complete Dulbecco's Modified Eagle Medium (DMEM, D6546, Sigma-Aldrich, UK) media supplemented with 1% (v/v) L-glutamine (G7513, Sigma-Aldrich, UK), 10% (v/v) Fetal Bovine Serum (FBS) (F9665, Sigma-Aldrich, UK) and 1% (v/v) penicillin streptomycin (P4333) at 37 °C and 5% CO_2. The cell lines were tested negative for mycoplasma contamination by Mycoalert mycoplasma detection kit (Lonza). Cells were discarded after they reached passage 25 for MDA-MB-231 and passage 50 for MCF-7.

2.3.2. 3D in vitro model: alginate-gelatin hydrogel beads

Four different hydrogels were selected based on their stiffness (i.e. soft, stiff) and gelatin concentration (i.e. low and high adhesive ligand content), and further used for 3D cell culture studies (Table 3). Briefly, cells were detached using trypsin (3 min, 37°C) and centrifuged (3 min, 600g). Cell pellets were gently resuspended in the hydrogel precursor solution using a MICROMAN E viscous pipette (M1000E, Gilson, UK) ensuring a single cell suspension. The cell-suspension was transferred in a sterile 1 mL syringe equipped with a 25G needle, and single droplets were ejected in a $CaCl_2$ solution allowing gelation (10 min, RT) and to obtain spherical hydrogel beads (Fig. 1C). To facilitate easy washing, hydrogel beads were collected using a sterile cell strainer (CSS-010-040, Biofil, UK) immersed in the $CaCl_2$ solution prior droplet generation [36]. After two washes in HBS (5 min, RT), the beads were immersed in complete cell culture media (Fig. SI1) and cultured at either pH 7.4 or pH 6.5 prepared with HEPES-PIPES buffered DMEM media (Section SI 1.7). Cells grown in this media were incubated at 37 °C and atmospheric CO_2 conditions; cell culture media was changed every 2 days to keep the target pH value (data not shown).

2.3.3. 3D dynamic model: Quasi vivo system

The Quasi vivo QV500 system (Kirkstall, UK) equipped with the Watson-Marlow 202U peristaltic pump was assembled following supplier's instruction (Fig. 1I). Prior to use, the QV500 PDMS chambers along with the reservoir, tubing and Luer connectors were sterilised with pure ethanol (20 min, RT) by perfusing the whole system (flow rate 2 mL/min). After 20 min, ethanol solution was removed and the system was perfused with 1 × Phosphate buffered saline (PBS) sterile solution (1 h, RT) and finally with complete cell culture media (overnight, 37 °C, 5% CO_2). Cells embedded in hydrogel beads were transferred into individual chamber connected to their respective reservoir system (Fig. 1I). Each experiment was performed placing the system inside the incubator and setting flow rate to 500 µL/min [37], to guarantee physiological dynamic conditions and transmit mechanical forces. To ensure uniform flow by the peristaltic pump, the chambers are connected to the pump through a reservoir (and not directly) that acts as a flow rectifier to convert peristaltic flow into a smooth flow [38].

2.4. Cell proliferation and viability

2.4.1. Cell proliferation: Alamar blue assay

Alamar blue assay (Deep Blue Cell Viability™ Kit 424701, Biolegend) was used to analyse cell proliferation at different time points (i.e. day(s) 1, 4, 7 and 14) without disrupting samples. A 10% (v/v) deep blue solution was diluted in complete cell culture media (pH 7.4) and added to each sample (refer to section SI I.8 for additional information on sample preparation). After 2 hours, 100 µL of samples were collected and read immediately using the Synergy-2 (Biotek) plate reader (Ex 530-570 nm / Em 590-620 nm). All intensity measurements at days 4, 7 and 14 were normalised with their respective reading at day 1. Measurements are reported as mean ± st.dev. of three independent experiments for static conditions (N=3). To validate the Alamar blue assay in the current 3D models, the linear range of assay was confirmed by measuring signals from increasing density of encapsulated cells (5,000, 10,000, 20,000 and 40,000) (Fig. SI3).

2.4.2. Cell viability: live/dead assay

Live dead assay has been routinely used to measure cell viability by quantifying the live and dead stain intensity [39–41]. Calcein-AM and ethylene homodimer (Live/Dead cytotoxicity kit L3224, Thermo-Fischer scientific) were diluted in sterile PBS at a

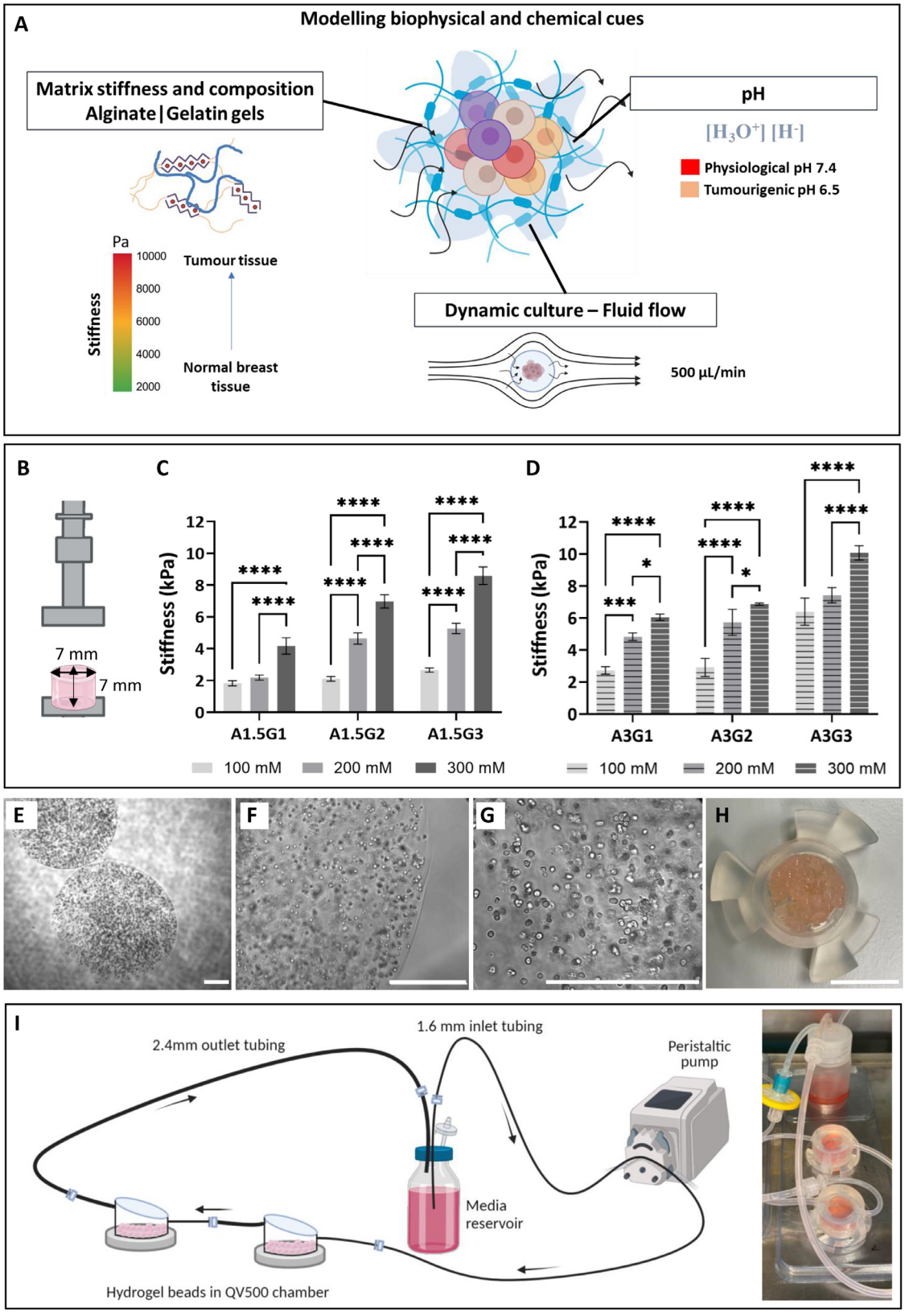

Fig. 1. Representation of independent biophysical cues included in 3D in vitro models. (A) Summary of biophysical and chemical properties engineered into precision 3D in vitro models, varying matrix stiffness (1.8 to 10 kPa), pH (7.4 and 6.5), and fluid flow (500 µL/min). (B-D) Mechanical properties of hydrogels: (B) Layout of compressive test (initial zero-stress) used to measure hydrogels stiffness (kPa). Stiffness values of 1.5% w/v (C) and 3.0% w/v (D) alginate concentrations with varying gelatin concentrations (1% w/v and 3% w/v) and calcium chloride crosslinking solution (100 mM, 200 mM and 300 mM). Values are represented as mean of average ± st.dev. of n=4, N=2 experiments. Tukey's post-hoc test was used for multiple comparisons after performing two-way ANOVA. P-values represented as $^{*}p \leq 0.05$, $^{**}p \leq 0.01$, $^{***}p \leq 0.001$, $^{****}p \leq 0.0001$. (E-G) Examples of brightfield images of MDA-MB-231 cells encapsulated in hydrogels beads (scale bars 500 µm) acquired with a 2 × (E), 10 × (F), and 20 × (G) objective. (H) Dynamic system: hydrogel beads encapsulating cells cultured in QV-500 chamber (scale bar 10 mm). (I) Schematic layout of QV500 chambers, 1.6 mm and 2.4 mm tubing, 30 mL media reservoir connected with peristaltic pump (left) along with actual image of the system (right). (Created with BioRender.com)

Table 2
Antibody dilutions for selected isotype control, primary and secondary antibodies.

Marker	Isotype control	Primary antibody	Secondary antibody
CD44	APC Rat IgG2b, κ Isotype Ctrl (400611, BioLegend)	APC anti-mouse/human CD44 Antibody (103012, BioLegend),	N/A
Dilution	**1:800**	**1:800**	N/A
CD24	Alexa Fluor® 488 Mouse IgG2a, κ Isotype Ctrl Antibody (400233, BioLegend)	Alexa Fluor® 488 anti-human CD24 Antibody (311108, BioLegend)	N/A
Dilution	**1:20**	**1:20**	N/A
E-cadherin	Mouse IgG1, kappa monoclonal (ab170190, Abcam)	Mouse IgG1 anti human E-Cadherin antibody (ab1416, Abcam)	BV786 Rat Anti-Mouse IgG1, (742480, BD)
Dilution	**1:100**	**1:100**	**1:150**
Vimentin	Rat IgG2A APC Isotype control (IC006A, R&D systems)	APC Rat anti-human Vimentin (IC2105A, R&D systems)	N/A
Dilution	**1:10**	**1:20**	N/A

final concentration of 2 μM and 4 μM, respectively. Prior image acquisition, samples at day 7 and day 14 were incubated in the dark with this solution (40 min, RT). Images were acquired using the fluorescent inverted microscope (details in Section 2.9) using the objective 10×.

2.5. B-CSCs and EMT marker expression: flow cytometry

Marker expression (i.e. CD44, CD24, E-cadherin and vimentin) was analysed by flow cytometry (BD Fortessa X-20). Cells cultured in two-dimensional (2D) tissue-culture plates (TCP) plates were used as control. At each time point, cells were washed with 1 × PBS and incubated with cell dissociation buffer (13151014, Gibco, 10 min, RT) to avoid disruption of membrane bound proteins during cell detachment [42]. Cells cultured in hydrogels were recovered by dissolution of alginate beads through addition of a calcium sequestering buffer (100 mM HEPES and 500 mM Trisodium citrate dehydrate in 1 × PBS) as previously described by Rios de la Rosa et al. [43]. For the preparation of samples to detect cell surface markers, cell pellet (600 g, 5 min, RT) was gently resuspended in blocking buffer (5% (v/v) FBS in 1 × PBS) and incubated for 30 minutes on ice. For the detection of intracellular markers (i.e. vimentin), samples were fixed with 4% paraformaldehyde (1004968350, Sigma-Aldrich, UK, 10 min, RT), followed by n=3 washes with 1 × PBS, and a final permeabilisation step with 0.1% w/v Saponin (47036, Sigma-Aldrich, UK) in blocking buffer (30 min, RT). All cells were then incubated on ice with primary antibody (45 min) and secondary antibodies (30 min) at concentrations described in Table 2. Finally, for dead cell exclusion during flow cytometry measurements, all cells were incubated with 1μg/mL of 4′,6-diamidino-2-phenylindole (DAPI) solution in 1 × PBS (5 min, RT), then washed with 1 × PBS and resuspended in 1 × PBS for further measurements. All the markers were examined separately, apart from CD44 and CD24. FlowJo software (v10.8.0, BD) was used to analyse data, gate single live cells and obtain measurements on median fluorescence intensity (MFI) and number of cells positive for each marker. The median intensity of the marker was normalised by its respective isotype control for every sample and then plotted as an average of N=3 independent experiments.

2.6. ALDH expression: Aldefluor assay

Aldefluor assay (Stemcell Technologies) was used to measure ALDH expression, as per the supplier's instructions. Briefly, cells (1×10^6 cells/mL) suspended in Aldefluor buffer were treated with 5 μL of ALDH substrate Bodipy-aminoacetaldehyde (BAAA) (45 min, 37°C). For negative control, half of this mix was simultaneously treated with 5 μL of ALDH inhibitor DEAB (1.5 mM). To exclude dead cells from measurements, cells were incubated with 7-AAD (420403, Biolegend, 10 min, RT) prior to their assessment in BD Fortessa X-20 flow cytometer. The gates for $ALDH^+$ cells were sorted based on the DEAB negative control of the respective sample. All data were analysed using FlowJo software (v10.8.0, BD).

2.7. Analysis of cell aggregates: size and shape

Live/dead images of cells in hydrogel beads were acquired using the fluorescent inverted microscope (details reported in Section 2.9) placing each hydrogel bead between a glass slide and coverslip for the acquisition of a single focus image. ImageJ (v1.52a) was used to identify and measure the area (μm^2) and circularity of cell aggregates (approx. 200 aggregates/condition, Section SI 1.9).

2.8. Principal component analysis

Principal component analysis (PCA) was performed on EMT marker expression (vimentin and E-cadherin) and "stemness" marker positivity ($CD44^+/CD24^-$ and $ALDH^+$) of cells cultured in different conditions, namely: 1) pH 7.4 static, 2) pH 7.4 dynamic 3) and pH 6.5 static. The data was processed using PCA analysis function on GraphPad prism (v9.2.0). Two principal components (PC1 and PC2) from the obtained analysis were selected by Kaiser's rule (> 1) and used to graph the PC score plot (PC1 vs PC2).

2.9. Image acquisition and analysis

Images were acquired using a fluorescent inverted microscope (Leica DMI6000, Leica Microsystems, UK) coupled with a 5.5 Neo sCMOS camera (Andor, UK). The μManager software (v.1.46, Vale Lab, UCSF, USA) was used to control both microscope and camera, as well as to capture images. For Live dead assay, stained cells were acquired at 10 × objective (PL 10 × /0.3 PH1, Leica) using filter cubes I3 (Ex/Em 450/515 nm) and N2.1 (Ex/Em 515/590 nm) to detect calcein (live cells) and ethylene homodimer (dead cells), respectively. Z-stacks were acquired with a set 20 μm z-step and were post-processed using ImageJ (v1.52a) to obtain maximum intensity projection images and to remove background noise. Percentage of live and dead cells was calculated using maximum projections (n=10 images) for each sample and at each time point.

High-resolution electron micrographs of selected alginate formulations were obtained using a Supra 40 (Zeiss, Germany) field emission electron microscope (FESEM) applying 5 kV voltage acceleration and collecting the secondary emission. Samples were prepared as previously described, snap frozen and freeze-dried. Before

Table 3
Properties of selected hydrogels: Adhesion ligand density, polymer concentration and stiffness of the four selected hydrogel groups. The hydrogels were named based on combination their stiffness (So- Soft or St-Stiff) and gelatin concentration (L- low or H- high).

Hydrogel mimicking breast tissue	Sample ID [±]	Crosslinking solution [§]	Adhesion ligand content [*]	Density [**]	Stiffness [§§]
So-L	A1.5G1	100	Low	Low	1.8 ± 0.2
So-H	A1.5G3	100	High	Medium	2.4 ± 0.1
St-L	A3G1	300	Low	Medium	6.1 ± 0.2
St-H	A3G3	300	High	High	10.1 ± 0.5

[±] Hydrogel precursor formulation (from Table 1);
[§] Calcium Chloride ($CaCl_2$ (aq.), mM);
[*] Gelatin concentration and
[**] Total concentration of polymers (from Table 1).
[§§] Compressive moduli (kPa).

measurements samples were coated with 4 nm Pt80/Pd20 alloy by plasma sputtering.

2.10. Statistical analysis

Significance of cell proliferation and flow cytometry data was analysed with one-way analysis of variance (ANOVA), whereas significance among hydrogels stiffness was analysed with two-way ANOVA. Non-parametric one-way ANOVA (Kruskal Wallis) was used to test significance amount for cell aggregate size and shape. The details of analysis and the post-hoc test used is mentioned below the respective figures. All analyses were performed using GraphPad Prism (v9.1.0). P-values were set at four different significance levels: $p < 0.05$ ($^{*}p \leq 0.05$, $^{**}p \leq 0.01$, $^{***}p \leq 0.001$, $^{****}p \leq 0.0001$).

3. Results

3.1. Modelling biophysical and chemical cues in vitro

Biophysical and chemical cues of breast TME were engineered using a bottom-up tissue engineering approach by controlling: matrix stiffness and composition, pH, and fluid flow (Fig. 1A). Hydrogels with varying concentrations of alginate and gelatin (Table 1) were crosslinked with different concentrations of calcium chloride (100, 200 and 300 mM) to control composition, density and stiffness, and to match properties of human breast tissue during cancer progression. Compression tests (Fig. 1B) on a small library of hydrogels ($n = 18$) returned stiffness values in the range of 1.8-10.0 kPa (Fig. 1C,D). As expected, hydrogel stiffness increased proportionally with alginate and calcium chloride concentration (crosslinking density), as well as with gelatin concentration (final polymer density) (Fig. 1C,D).

After this analysis, four hydrogels were selected to represent different combination of stiffness (soft, stiff), adhesion ligand (low, high) and density (low, high) to investigate the role of these three independent parameters on human breast cancer cells (Table 3). Variations in architecture and physical properties of selected hydrogels (Table 3) was confirmed by EM images (Fig. 2) in both density and pore size. Of note, swelling tests of selected hydrogels in cell culture media with different pH did not evidence any difference up to 7 days, as expected (Fig. SI2).

MDA-MB-231 and MCF-7 cells encapsulated in alginate-gelatin hydrogel beads at the initial concentration of 2×10^6 cells/mL were observed to be homogenously distributed within the hydrogel beads (Fig. 1E-F) with mostly single cell suspension (Fig. 1G). As illustrated by the experimental layout for the dynamic model in Fig. 1H-I, the beads were placed in the QV500 chamber, and perfused at flow rate set to 500 µL/min allowing transmission of mechanical forces to encapsulated cells.

3.2. MDA-MB-231 proliferation is less sensitive to varying physico-chemical cues than MCF-7

MCF-7 and MDA-MB-231 cells were cultured in selected hydrogels (Table 3) in different media (pH 7.4 or 6.5), and in static or dynamic conditions, for up to 14 days. Cell proliferation and growth was measured at days 1, 4, 7 and 14 (Fig. 3, Alamar blue assay). Quantitative and qualitative assessment of cell viability was measured at day 7 and 14, quantifying percentage of live and dead cells (Fig. SI4-SI8, Live/Dead assay staining). Previous studies with alginate hydrogels have used variable end points to monitor cell growth ranging from day 3 to day 21 [43–45]. Since we observed saturation of growth during day 7-14 interval in most groups (data not shown), experiments were performed until day 14. When cultured in static conditions and at physiological pH, MCF-7 cells exhibited a 2-3-fold growth and a significantly higher growth rate ($p < 0.01$) in lower stiffness hydrogels compared to higher stiffness ones (Fig. 3A). Whereas MDA-MB-231 cells had a more quiescent (or low metabolically active) phenotype, showing a slow growth pattern with no significant differences dependent on stiffness (Fig. 3D). Live/Dead staining suggests that majority of MDA-MB-231 cells remain viable (> 85% live cells, static and pH 7.4) at both day 7 (Fig. SI4, SI6) and 14 (Fig. SI4, SI8), confirming a less proliferative and quiescent state. When the pH of cell culture media is reduced to 6.5, viability of MCF-7 was low at all time-points (Fig. 3B). This observation was confirmed by Live/Dead images with only a small group of viable cells at day 7 (Fig. SI4, SI5) and a large population of dead cells (> 70%) increasing with culturing time (day 14, Fig. SI4, SI7). On the contrary, MDA-MB-231 cells exhibited sustained proliferation (Fig. 3E) and remained viable when cultured at pH 6.5. Live/Dead staining confirmed presence of viable cells (>80%) at both day 7 (Fig. SI4, SI6) and day 14 (Fig. SI4, SI8). In comparison to static, dynamic culture (pH 7.4) generally did not lead to differences in cell viability among the stiffness groups. MCF-7 cells exhibited a 1.5-fold increase in higher stiffness hydrogels in dynamic culture (Fig. 3C), when compared to control (static, pH 7.4). This was also confirmed by analysis of Live/Dead images with a higher number of viable cells (>90%) in dynamic culture compared to static culture (>70%) in all groups at day 14 (Fig. SI4). All hydrogels embedding MDA-MB-231 cells (dynamic, pH 7.4) showed a slight and sustained increase in viability (Fig. 3F) when compared to static culture (Fig. 3E). Like MCF-7, a high % of viable MDA-MB-231 cells was measured in dynamic culture (>90%) at all time-points (Fig. SI4 and SI8). To summarize, all the results of cell proliferation in 3D models (Alamar blue, Fig. 3) indicate an intrinsic proliferative phenotype for MCF-7 cells as opposed to slowly proliferating MDA-MB-231 cells. Viability of MDA-MB-231 cells remains high (80-95%) in all hydrogels and conditions, whereas MCF-7 cells returned different viability (10% - 90%) highly dependent on the physical and chemical properties of the microenvironment, with lower pH values (i.e. 6.5) being the parameter that reduces the cell viability drastically within 7 days.

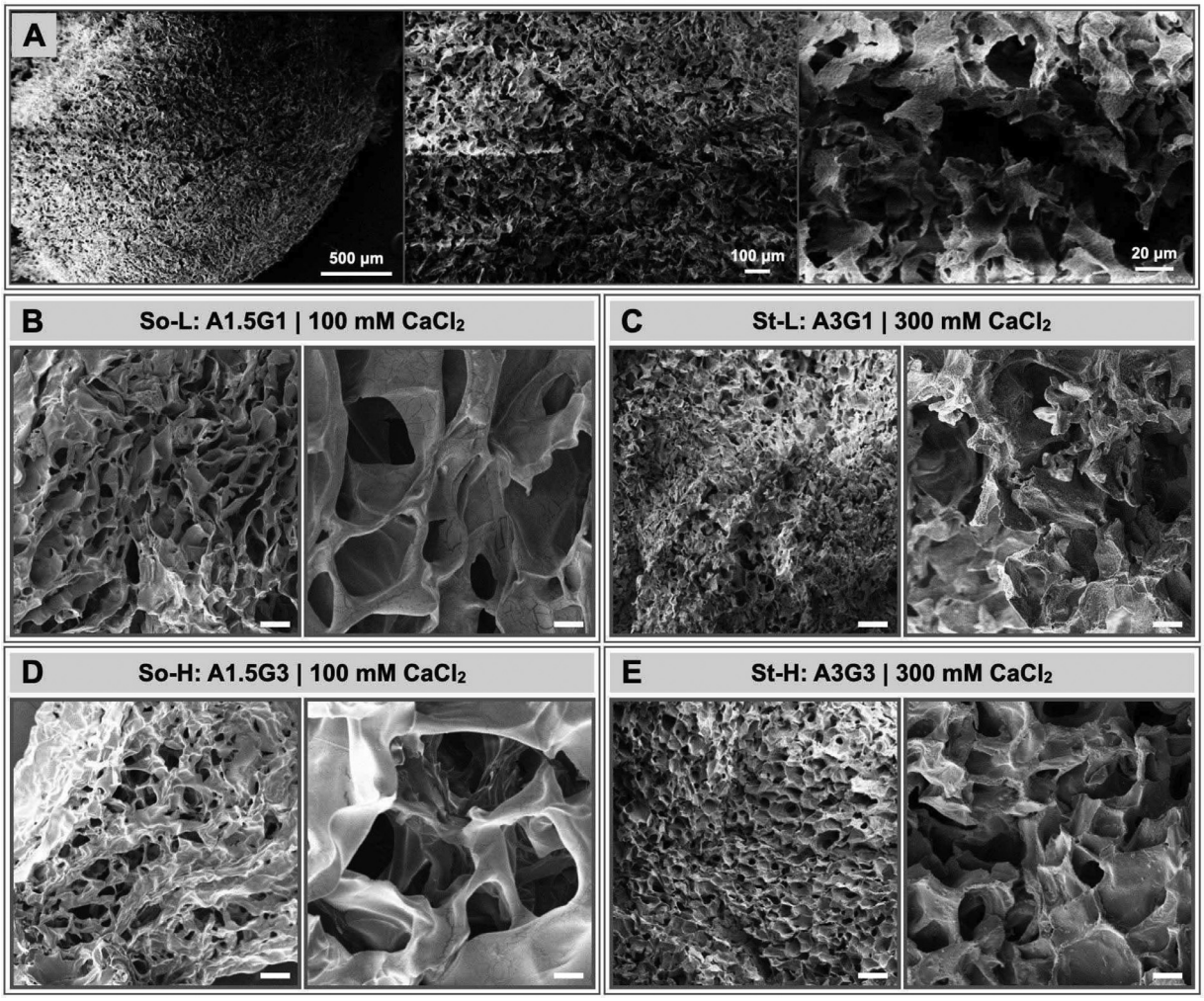

Fig. 2. SEM images of alginate-based dried samples. Example of alginate microbead (3% w/v, 300 mM $CaCl_2$) (A); and selected hydrogels (as reported in Table 3) with controlled features to mimic human breast tissue TME (B-E): 200 × magnification (left hand side, scale bars 100 µm), and 1,000 × magnification (right hand side, scale bars 20 µm). Measured average pore size: 22.7 ± 6.2 µm (So-L, B); 11.6 ± 2.2 µm (St-L, C); 17.1 ± 5.7 µm (So-H, D); 12.1 ± 2.2 µm (St-H, E).

3.3. Lower stiffness and dynamic cell culture permits for higher aggregate sizes in both cell lines

The two cell lines cultured in 3D alginate-gelatin hydrogels evidenced the formation of cell aggregates of mixed sizes over time (pH 7.4, static/dynamic), varying as function of the microenvironment (Fig. 4). Semi-quantitative analysis of cell aggregates was performed using Live/Dead images after 14 days of culture (Fig. 4B, C). Of note, cells did not form any aggregates when cultured in extracellular tumour acidosis conditions (i.e. pH 6.5). Since both single cells and cell aggregates were visible in the hydrogels at day 14, the percentage of aggregate population and sizes of aggregates formed were measured in acquired images. At pH 7.4, MDA-MB-231 cell lines showed significant increase in aggregate sizes when cultured in lower stiffness hydrogels (1.8-2.3 kPa) in both static and dynamic conditions ($p < 0.0001$, Fig. 4B). Likewise, percentage of aggregates present was higher in lower stiffness (~45%) than in higher stiffness (~20%) (Table SI1). In contrast MCF-7 significantly formed aggregates larger in size when cultured in lower stiffness but only when cultured in dynamic conditions (Fig. 4C). Surprisingly aggregate population percentage was similar across all hydrogel groups (~40-50%, Table SI1), indicating that the microenvironment mostly affected aggregate sizes in MCF-7. Generally, dynamic culture led to 1.2 to 1.4-fold increase in aggregate sizes when compared to static culture in both cell lines, consistent with the increased proliferation rate previously observed in dynamic culture (Fig. 4B, C). Also, MCF-7 exhibited larger aggregates than MDA-MB-231 (Fig. 4B vs C) supporting the former's observed proliferative phenotype compared to latter's quiescent phenotype (Fig. 3). Further, aggregate shape (circularity factor) was used as an indicator to identify cell invasiveness by measuring the extent of elongation and irregularity within cell aggregates (Fig. 5) [46]. MDA-MB-231 aggregates showed significantly lower circularity/more irregularity in hydrogels with high gelatin content and lower stiffness (Fig. 5E, $p < 0.001$). In addition, low circularity in high gelatin content was more pronounced when cells were cultured in dynamic conditions than static. As such, decrease in median circularity with increased gelatin content was almost 33% in lower stiffness groups ($p < 0.0001$), and 16% in higher stiffness (Fig. 5E, $p < 0.5$). However, no such change in circularity with increased gelatin content was found in MCF-7 cells (Fig. 5F). MDA-MB-231 aggregates with low circularity have more irregular shapes (Fig. 5C) than the aggregates formed by MCF-7 cells (Fig. 5D), whereas MCF-7 cells had larger aggregate size in general than MDA-MB-231 (Fig. 5A vs B).

3.4. E-CSCs and M-CSCs marker expression in MDA-MB-231

To assess B-CSCs dynamics in response to physico-chemical cues we measured M-CSC ($CD44^+/CD24^-$, vimentin) and E-CSC

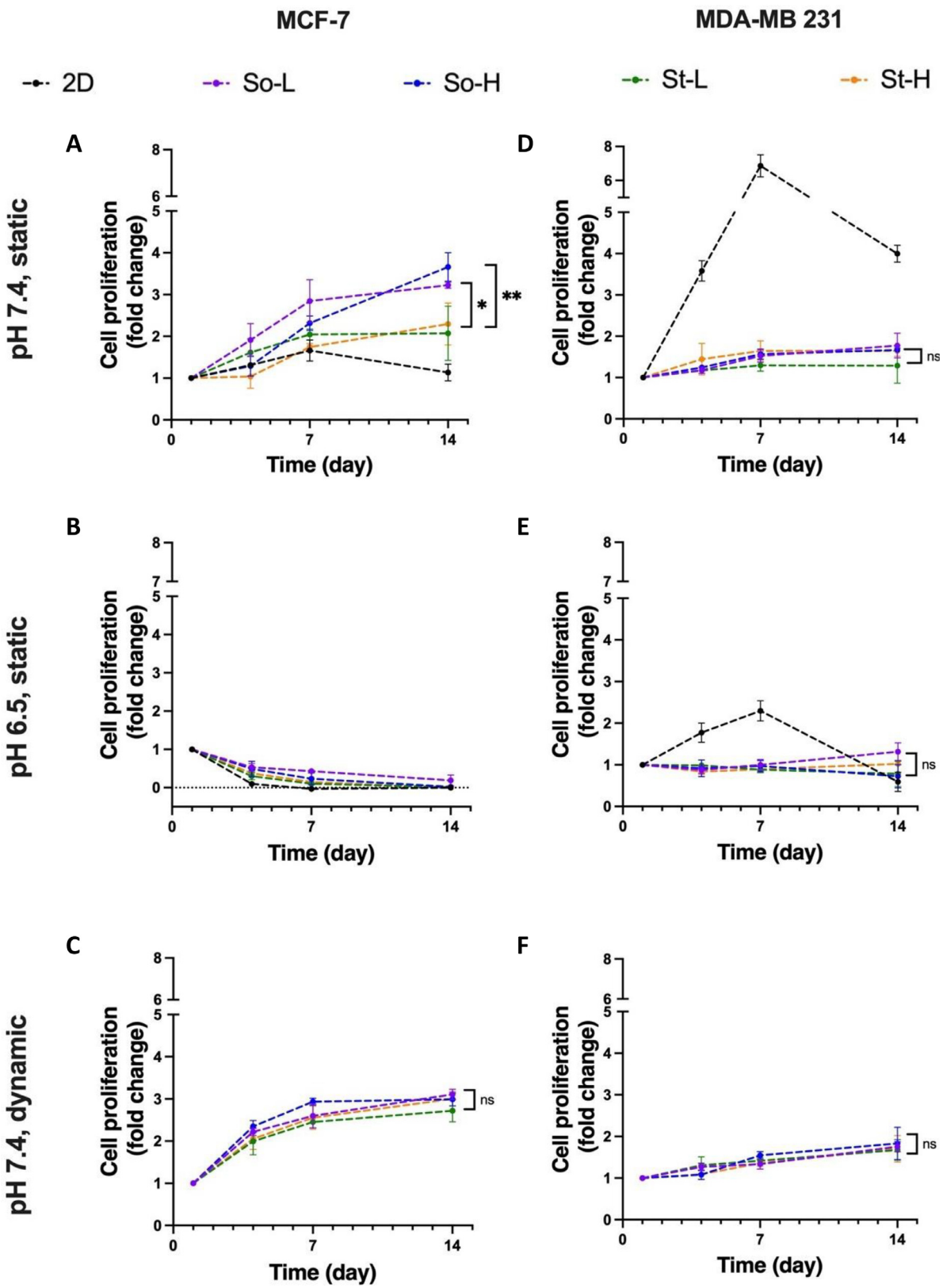

Fig. 3. Normalised cell proliferation of MCF-7 and MDA-MB-231 cells in pH 7.4 static culture (A, D), pH 6.5 static culture (B, E), and pH 7.4 dynamic culture (C, F) respectively on day 1, 4, 7, and 14. Lines represents cells cultured in 2D (control, black), So-L (purple), So-H (blue), St-L (green), St-H (orange). To better visualise relative cell growth, values reported on each graph were obtained by dividing relative fluorescence unit values by that of day 1 values at each time point. Values are represented as average ± st.dev. of n=3, N=3 experiments for static conditions and n=1, N=3 experiments for dynamic conditions performed on different days. Tukey's post-hoc test was used for multiple comparisons after performing one-way ANOVA. P-values are set as $^{*}p \leq 0.05$, $^{**}p \leq 0.01$.

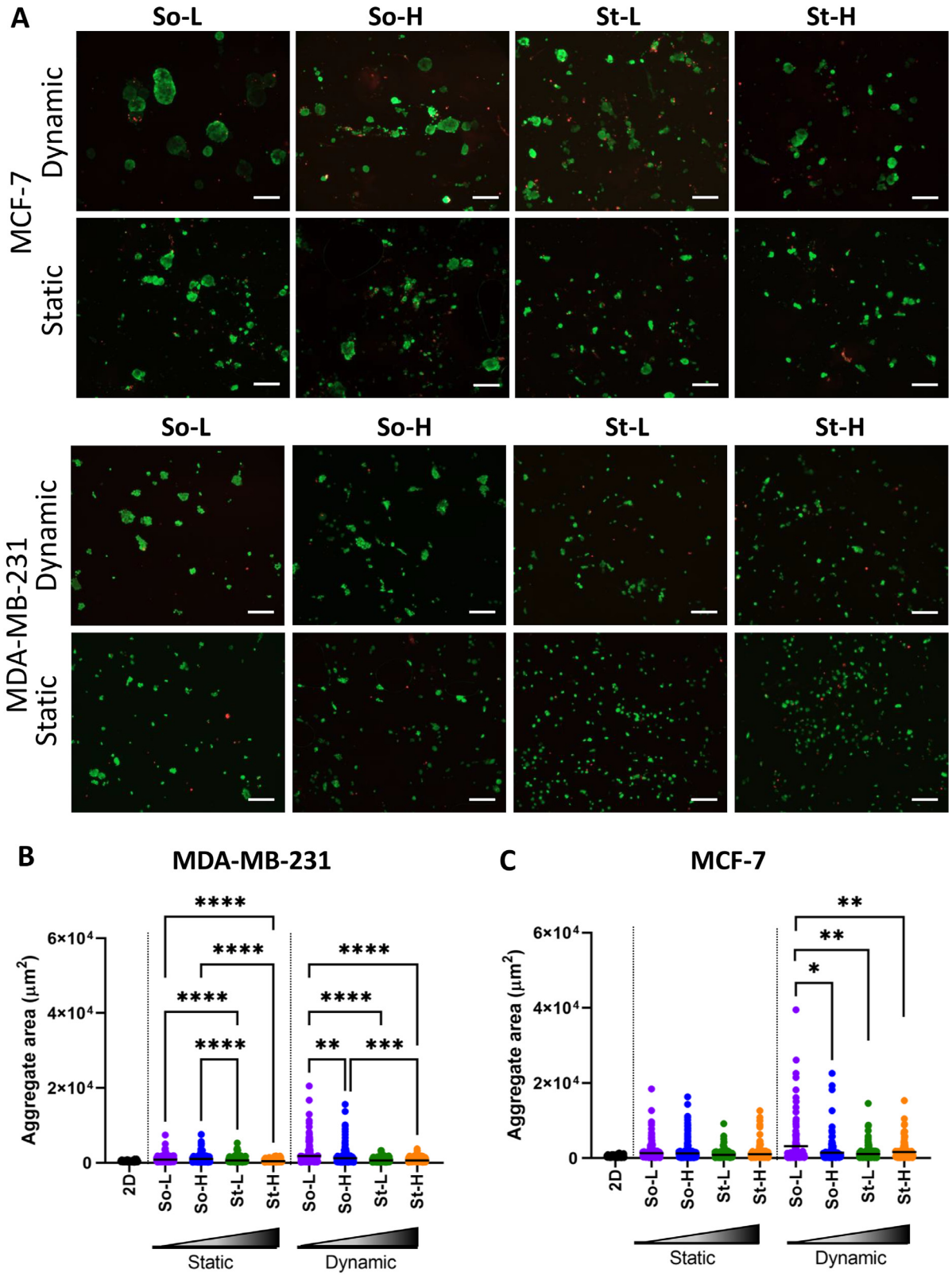

Fig. 4. (A) Live (green) /Dead (red) images of MCF-7 and MDA-MB-231 aggregates formed in selected four hydrogels cultured in static or dynamic conditions at physiological pH (pH = 7.4) (Scale bars: 200 μm). Quantification of aggregates area (μm^2) formed in four hydrogel groups at pH 7.4 in either static or dynamic condition for (B) MDA-MB 231 aggregates and (C) MCF-7 aggregates. Values are represented as dot plot and mean values for a minimum of n = 200 aggregates/objects in each condition tested for both cell lines. One-way non-parametric ANOVA test (Kruskal-Wallis) was run followed by Dunn's multiple comparison post-hoc test to examine significance. P-values represented as $^*p \leq 0.05$, $^{**}p \leq 0.01$, $^{***}p \leq 0.001$, $^{****}p \leq 0.0001$.

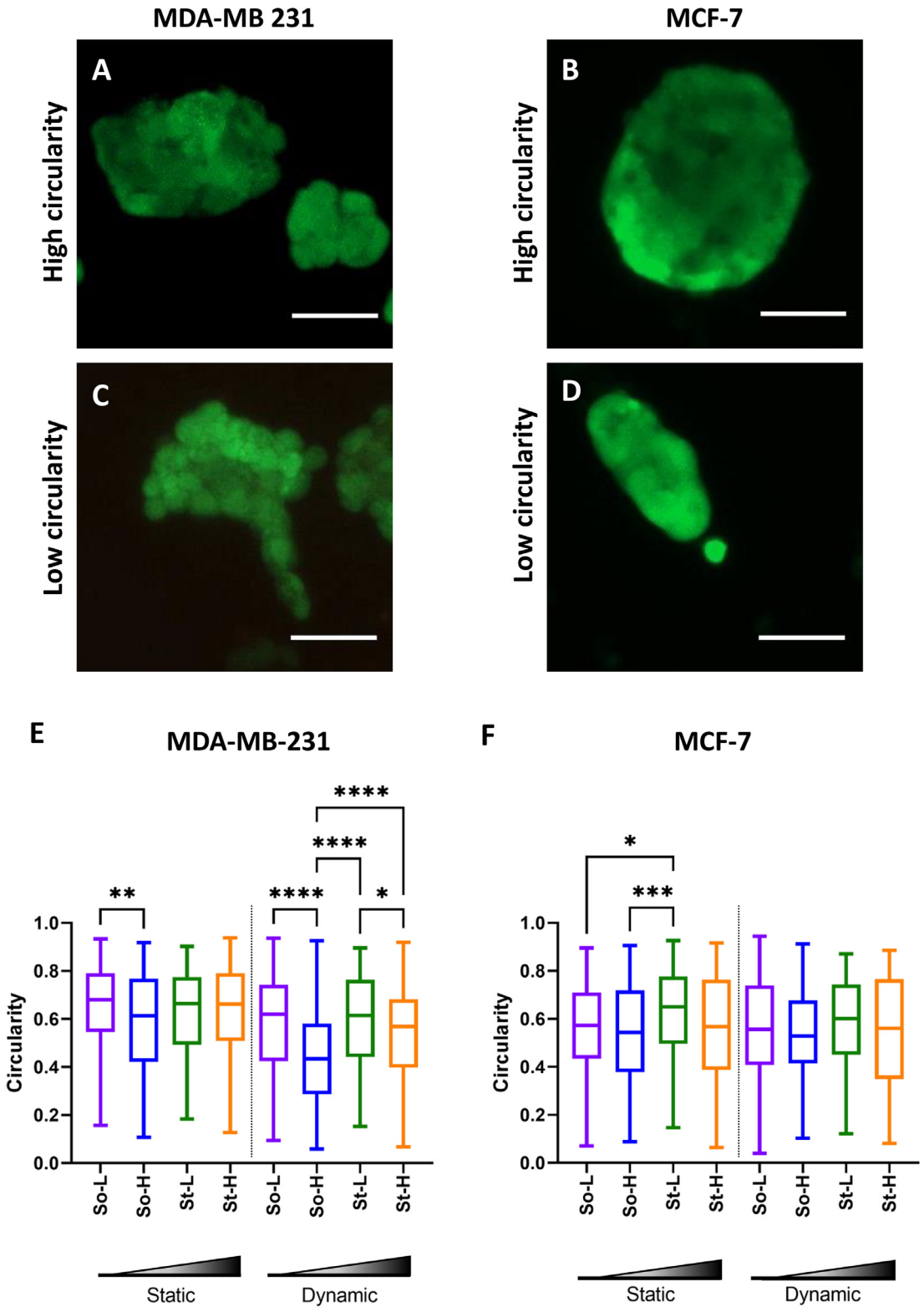

Fig. 5. Examples of cell aggregates stained with calcein formed at day 14 within hydrogels with high and low circularity values: MDA-MB-231 with (A) high and (C) low circularity, and MCF-7 with (B) high and (D) low circularity. (Scale bars 50 μm). Quantification of circularity of (E) MDA-MB-231 and (F) MCF-7 cell aggregates represented as box and whiskers plot consisting of the maximum, third quartile, median, quartile and minimum values (from top to bottom) of each experimental condition tested, this representation was selected to better visualise distribution of circularity for each sample. Values were obtained from quantification of a minimum of n = 200 cell aggregates. One-way non-parametric ANOVA test (Kruskal-Wallis) was run followed by Dunn's multiple comparison post-hoc test to examine significance. P-values represented as $^{*}p \leq 0.05$, $^{**}p \leq 0.01$, $^{***}p \leq 0.001$, $^{****}p \leq 0.0001$.

markers ($ALDH^+$, E-cadherin) expression through flow cytometry on day 7 of culture (Fig. 6). Day 7 was chosen to study marker expression, as all conditions (pH 7.4 static, pH 6.5 static and pH 7.4 dynamic) in both cell lines had at least 40% viable cells up until this time point. On 2D controls (TCP plates), MDA-MB-231 cells are known to be mesenchymal with majority of cells being $CD44^+/CD24^-$ with high vimentin expression (> 90%) and very low ALDH positivity (~3%) (Fig. 6C-E, H-J). Interestingly, with increase in stiffness there is a significant decrease of almost 75% in $CD44^+/CD24^-$ population ($p < 0.0001$) and lower vimentin expression ($p < 0.01$) (Fig. 6A, B). Of note, CD44 positivity remains unaffected but CD24 positivity increases with stiffness (Fig. SI10). This is coupled with slight but significant two-fold increase in ALDH positivity ($p<0.001$) and 1.5-fold increase in E-cadherin expression ($p < 0.05$) (Fig. 6F, G). Increase in hydrogel stiffness and at physiological pH led to decreased M-CSC markers and increased E-CSC markers in MDA-MB-231 cells cultured in 3D, whereas 2D controls mainly expressed M-CSC markers. On contrary to pH 7.4, and when cells were cultured in extracellular tumour acidosis conditions (i.e. pH 6.5), a sustained M-CSC phenotype was confirmed in higher stiffness hydrogels with negligible decrease in $CD44^+/CD24^-$ cells and increased vimentin expression ($p < 0.5$) (Fig. 6A, B). Surprisingly, E-CSC marker ALDH positivity also increased 3 to 4-fold in higher stiffness ($p < 0.0001$) (Fig. 6F). Overall, acidic pH led to sustained M-CSC phenotype and also an increase in ALDH positivity in higher stiffness compared to lower. When MDA-MB 231 cells are perfused (pH 7.4), $CD44^+/CD24^-$ phenotype is sustained along with vimentin expression but there is significantly less ALDH positivity (~1%) (Fig. 6A, B, F). Such results suggest that dynamic culture conditions and mechanical forces might enrich M-CSCs over E-CSCs.

3.5. E-CSC and M-CSC marker expression in MCF-7

MCF-7 cells are luminal type cells which are comparatively less invasive and with majority of population expressing epithelial characteristics, i.e. low expression of vimentin and high of E-cadherin. The analysis for B-CSC markers on cells cultured on TCP exhibits negligible $CD44^+/CD24^-$ and $ALDH^+$ suggesting this cell line has low stem cell pool (Fig. 7C-E, H-J). MCF-7 cells cultured in 3D models (static conditions, pH 7.4) evidence a clear decrease in E-cadherin expression, notably the E-cadherin expression is negatively correlated with increase in hydrogel stiffness ($p < 0.001$, Fig. 7G). At the same time, a slight but significant increase ($p < 0.01$) is observed in $CD44^+/CD24^-$ expression (increase from ~2% positivity to ~4% positivity), with a positive correlation to hydrogel stiffness (Fig. 7A). Low pH and high stiffness hydrogels (A3G1 and A3G3) were seen to be associated with increase in $ALDH^+$ from 2% to 5% ($p < 0.0001$) accompanied with negligible E-cadherin expression (Fig. 7F, G). Similar to MDA-MB 231, dynamic culture shows increased $CD44^+/CD24^-$ but low $ALDH^+$ along with a slight increase in vimentin expression, clearly favouring M-CSC markers (Fig. 7A, B). Unlike MDA-MB-231 cells, this cell line exhibits no clear increase or decrease in E-CSC or M-CSC markers but rather changes in individual marker expression. Increased stiffness and acidic pH here as well are related to slight increase in both $CD44^+/CD24^-$ and $ALDH^+$ cells suggesting a role for this kind of microenvironment in increased stem cell pool.

3.6. Principal component analysis (PCA) of B-CSC markers

These results suggest that B-CSC equilibrium is influenced by the physico-chemical characteristics of the TME. To analyse and visualise data in a comprehensive manner, PCA was used to correlate markers expression ($CD44^+/CD24^-$, $ALDH^+$, vimentin and E-cadherin) with the microenvironment. To assess which physico-chemical cue most affects CSC markers, the same PC plot was presented with different colour coding based on stiffness (low and high stiffness group, Fig. 8A,D), gelatin content (low and high gelatin, Fig. 8B,E), or physico-chemical environment (pH 7.4 static, pH 6.5 static, pH 7.4 dynamic, Fig. 8C,F). From the PC plots, it is apparent that cells cultured in lower stiffness hydrogel cluster separately than those in high stiffness (light blue vs dark blue, Fig. 8A,D) for both the cell lines. However, no such clustering was observed when cells were cultured in different gelatin content (Fig. 8B,E). Furthermore, cells cultured in different physico-chemical factors (static/dynamic culture, pH 7.4/pH 6.5) exhibit partial clustering (red vs blue vs green, Fig. 8C,F). Interestingly, we also noticed a linear pattern of increasing hydrogel stiffness in each of these clusters (Fig. 8C,F) from point Ax (lower stiffness low gelatin) to Dx (high stiffness high gelatin), where 'x' represents the physico-chemical microenvironment, i.e. 1) pH 7.4 static, 2) pH 7.4 dynamic, and 3) pH 6.5 static culture. Observed clustering for both cell lines suggests that biophysical and chemical environment influences B-CSCs marker equilibrium.

4. Discussion

Traditional 2D *in vitro* models have been used to study cell-cell and cell-matrix interactions from early to late-stages of cancer progression, as well as to test efficacy of treatments. However, they fail to incorporate properties of tissues, such as 3D architecture of ECM, its physico-chemical properties, and transmission of mechanical forces and interstitial fluid flow. Animal models have the required *in vivo* complexity to study the dynamics of pathologies, being successful in mimicking most aspects of the human TME such as stromal components, vascularisation and tissues cross-talk. However, in these models the control over variations of TME properties with required resolution cannot be easily achieved. In the past two decades, 3D *in vitro* models have been successfully used to mimic physiological variations, replacing 2D models, in many applications like disease modelling [47,48], disease prognosis [49], drug discovery [32] and clinical applications [50]. In this study, we have engineered precision 3D *in vitro* models using hydrogels mimicking the breast TME to encapsulate human breast cancer cells, and a perfusion system to transmit mechanical forces. A small library of alginate-based hydrogels was characterized, and four hydrogels mimicking stiffness of normal breast tissue (1- 2 kPa) and breast tumour tissue (up to a 5-fold increase in stiffness, i.e. 6-10 kPa [19]) were selected (Table 3). Selected alginate-based hydrogels have intrinsic bio-compatibility, easy control over gelation, architectural and mechanical features (Fig. 2, SEM) similar to breast tissue ECM [51]. As shown in Fig. 2, hydrogels have density proportional to polymer concentration (So-L < So-H ~ St-L < St-H, as expected and reported in Table 3); moreover, smaller pores were observed with increase in $CaCl_2$ concentration used to form hydrogels. Other biomaterials like collagen (major ECM component), hyaluronic acid and Matrigel have been previously used in many studies for 3D cell encapsulation. However, both pure collagen hydrogels [52] and Matrigel [53] have poor mechanical properties with higher degradation rate; moreover, although they are rich in cell adhesive moieties and growth factors, high batch-to-batch variation is reported due to the nature of their sourcing. In our previous study, we have shown that alginate-based hydrogels allow gentle recovery of live cells [43], of particular interest for many assays (e.g. FACS analysis and/or sorting) because of the gentle dissolution process. The hydrogels presented in this study provide a better alternative to collagen or other natural and synthetic hydrogels reported in literature, which require enzymatic and me-

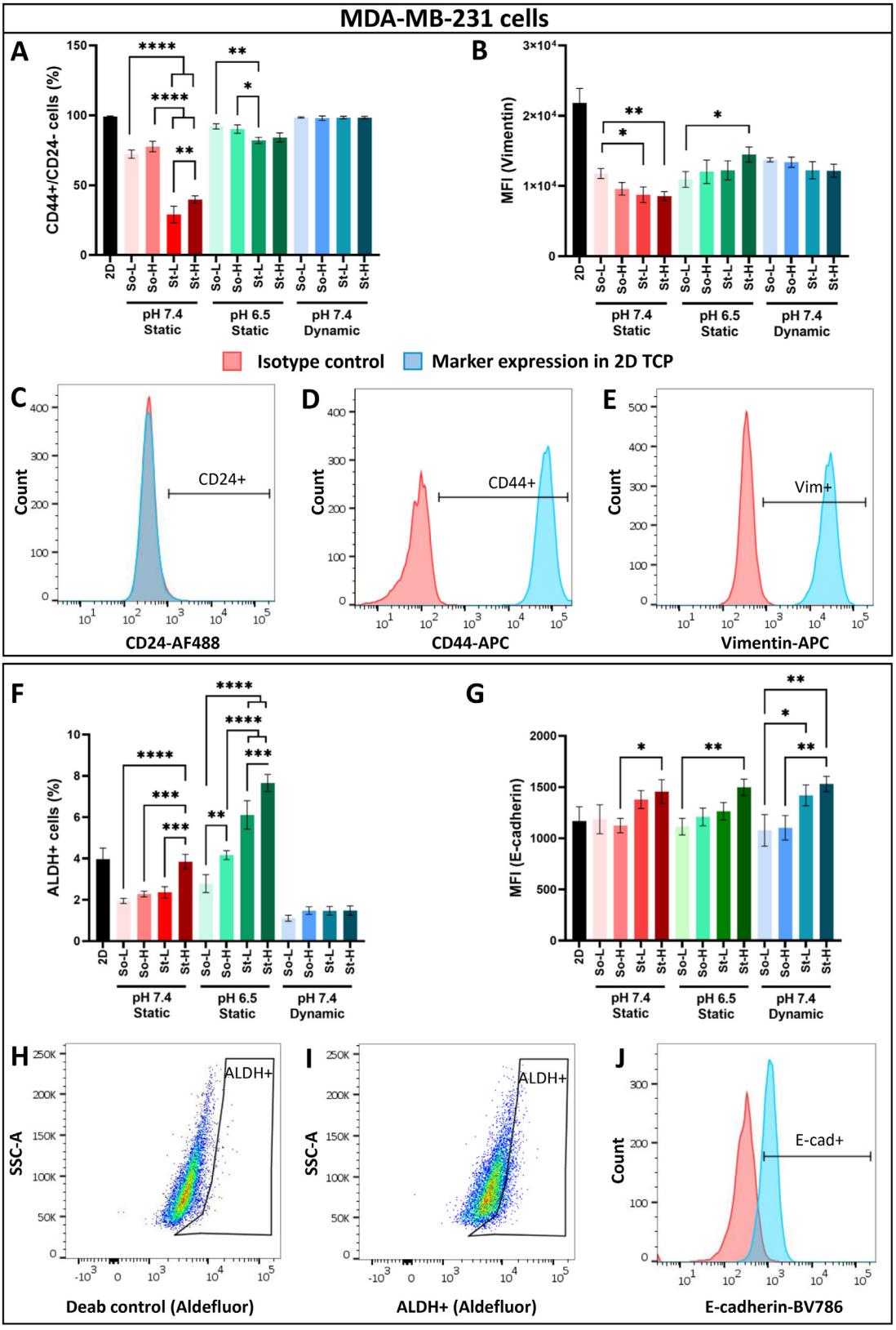

Fig. 6. Flow cytometry quantification in MDA-MB-231 cells of (A) $CD44^+/CD24^-$ cells (%), and (B) median fluorescence intensity (MFI) of Vimentin-APC (fluorescent arbitrary units, a.u.) for characterisation of M-CSCs in various conditions. Example of gating with isotype control of (C) $CD24^+$, (D) $CD44^+$, (E) $vimentin^+$. (F) Quantification of $ALDH^+$ cells (%) and MFI of (G) E-cadherin-BV786 (a.u.) for characterisation of E-CSCs. (H) Example of gating of ALDH+ cells with negative DEAB control and (I) aldefluor reagent. (J) Example of gating with isotype control of E-cadherin. Further representation of gating for $CD44^+/CD24^-$ and $ALDH^+$ in various conditions is shown in Fig. SI11. The labels in graphs are denoted as 2D (2D TCP plate), So-L, So-H, St-L and St-H. The microenvironmental in which these gels are cultured is mentioned below the labels as pH 7.4 static, pH 6.5 static, and pH 7.4 dynamic culture. Values are represented as mean and st.dev. of N=3 independent experiments. Tukey's post-hoc multiple comparison test was performed after one-way ANOVA. P-values represented as $^*p \leq 0.05$, $^{**}p \leq 0.01$, $^{***}p \leq 0.001$, $^{****}p \leq 0.0001$).

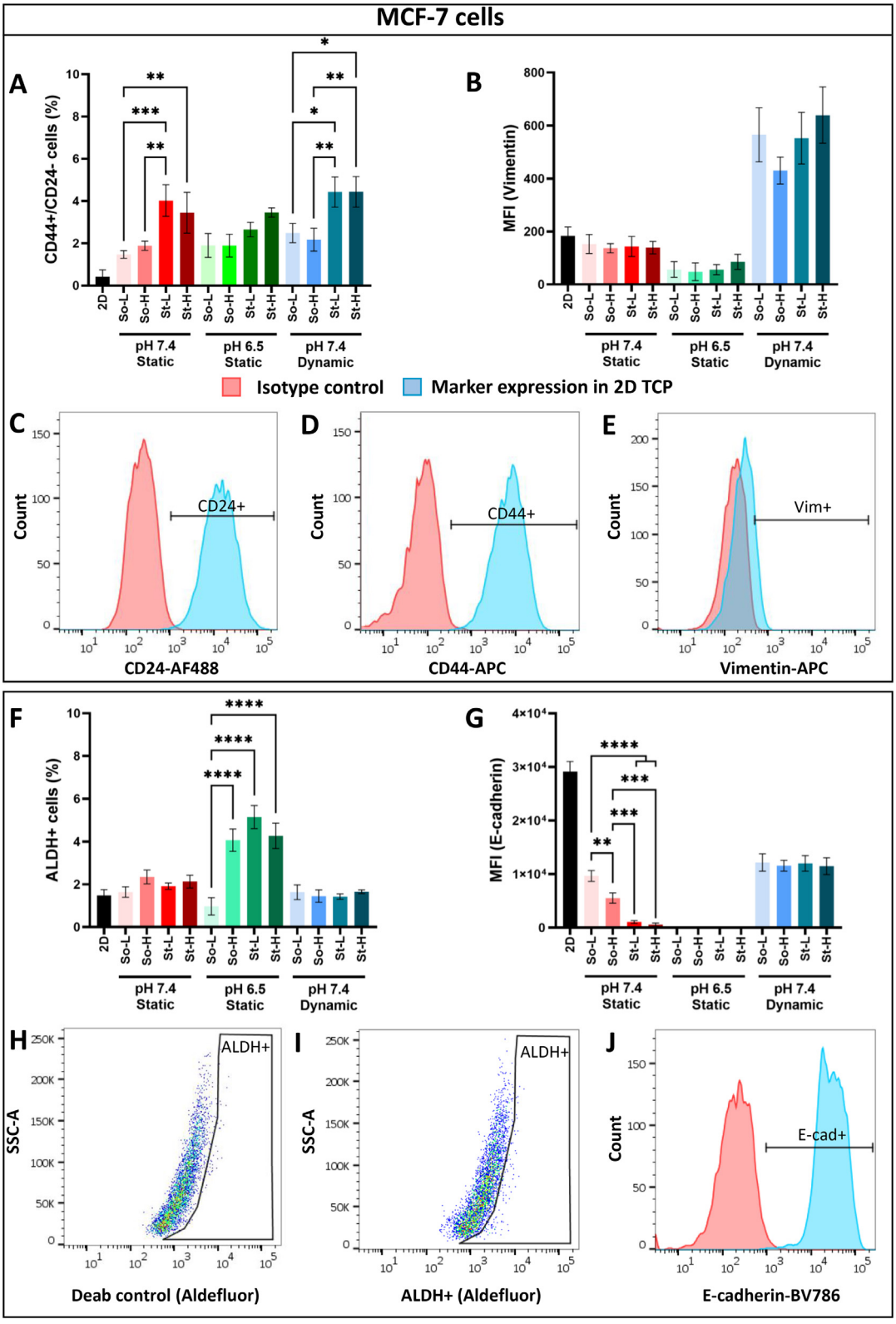

Fig. 7. Flow cytometry quantification in MCF-7 cells of (A) $CD44^+/CD24^-$ cells (%), and (B) median fluorescence intensity (MFI) of vimentin-APC (fluorescent arbitrary units, a.u.) for characterisation of M-CSCs in various conditions. Example of gating with isotype control of (C) $CD24^+$, (D) $CD44^+$, (E) $vimentin^+$. (F) Quantification of $ALDH^+$ cells (%) and MFI of (G) E-cadherin-BV786 (a.u.) for characterisation of E-CSCs. (H) Example of gating of ALDH+ cells with negative DEAB control and (I) aldefluor reagent. (J) Example of gating with isotype control of E-cadherin. Further representation of gating for $CD44^+/CD24^-$ and $ALDH^+$ in various conditions is shown in Fig. SI13. The labels in graphs are denoted as 2D (2D TCP plate), So-L, So-H, St-L and St-H. The microenvironmental in which these hydrogels are cultured is mentioned below the labels as pH 7.4 static, pH 6.5 static, and pH 7.4 dynamic culture. Values are represented as mean and st.dev. of N=3 independent experiments. Tukey's post-hoc multiple comparison test was performed after one-way ANOVA. P-values represented as $^*p \leq 0.05$, $^{**}p \leq 0.01$, $^{***}p \leq 0.001$, $^{****}p \leq 0.0001$).

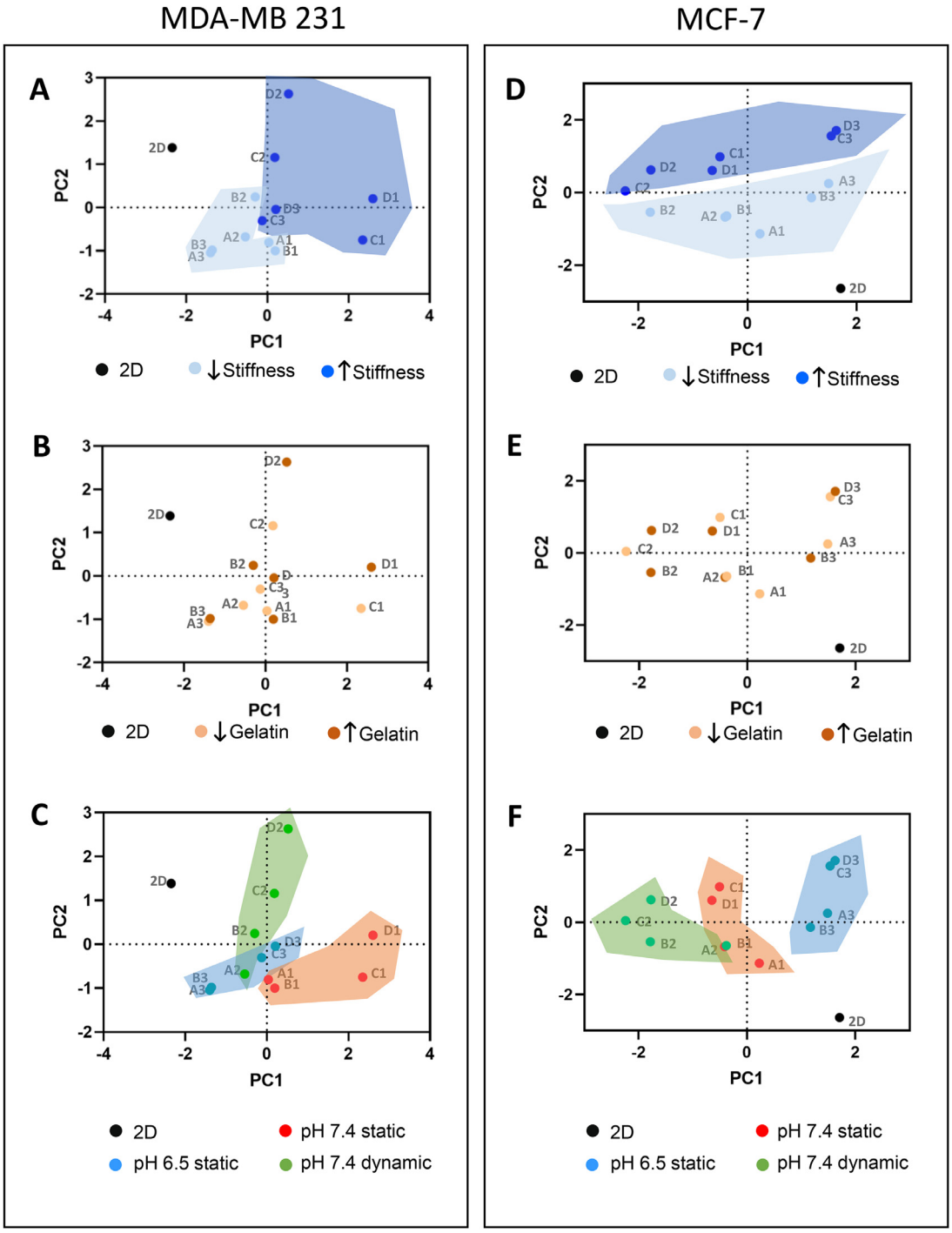

Fig. 8. Principal component analysis (PCA) of B-CSC marker expression in different in vitro models presented in the study (i.e. conventional 2D pH 7.4 static, 3D pH 7.4 static, 3D pH 6.5 static and 3D pH 7.4 dynamic) for (A, B, C) MDA-MB 231 and (D, E, F) MCF-7. Data are represented by PC score plot (PC2 vs PC1) where eigenvalue for PC1 = 1.864 and PC2 = 1.258 for MDA-MB 231 and PC1 = 1.99 and PC2= 1.382 for MCF-7. The data points represent hydrogel type (A: So-L, B: So-H, C: St-L, D: St-H) and physicochemical cue (1- pH 7.4 static, 2- pH 7.4 dynamic, 3- pH 6.5 static). The plots are colour coded for: (A, D) 2D, low stiffness groups and high stiffness groups, (B, E) 2D, low gelatin groups and high gelatin groups, and (C, F) 2D, 3D pH 7.4 static, 3D pH 6.5 static and 3D pH 7.4 dynamic culture.

chanical degradation, reducing efficacy of cell retrieval (such as covalently crosslinked polyethylene glycol, polyacrylamide, etc.) [54].

To overcome the lack of cell-adhesive motifs on alginate, gelatin was included at different concentrations in the formulation allowing precise control over density and content of adhesion motif matching that of normal and tumour breast tissue ECM.

Hydrogels were then included in a milli fluidic perfusion system to mimic physiological interstitial fluid flow and transmit mechanical forces to cells, as *in vivo*. In this study, a flow rate of 500 µL/min was selected based on values reported in literature for breast cancer *in vitro* models [37]. Cell culture media was formulated to mimic extracellular pH of normal (pH 7.4) and tumour (pH 6.5) microenvironment. As per our knowledge, this is the first report that integrates different matrix stiffness, interstitial flow and pH to study the effect of the microenvironment on breast cancer phenotypes and B-CSC dynamics.

4.1. Cell proliferation

We found that growth in MCF-7 cell lines is more sensitive to changes in the physico-chemical microenvironment. The growth rate of MCF-7 was higher in physiological pH and lower stiffness whereas it decreased in a more tumorigenic environment (higher stiffness, denser matrix and low pH). In contrast, MDA-MB-231 cells showed slow and sustained growth rate in any conditions tested, exhibiting less sensitivity to changes in physico-chemical cues. Our observations are in accordance with existing literature that suggests MCF-7 spheroids have high intrinsic proliferation due to their near normal oxidative phosphorylation phenotype and are dependent on efficient use of available nutrients, which makes them sensitive to changes in nutrient supply (glucose, glutamate and pH). Whereas MDA-MB 231 cells, due to increased aerobic glycolysis, use nutrients quickly and inefficiently leading to a slower growth *in vitro* [55]. In line with our findings, MDA-MB 231 tumours *in vivo* contain lower proportions of viable cancer cells than tumour masses of MCF-7. However, *in vivo* MDA-MB 231 tumours were found to be larger than MCF-7 ones but this is mostly attributed to MDA-MB 231's motility and ability to invade areas with high resource availability which results in tumour expansion [55].

4.2. Cell aggregate size and shape

Both MDA-MB-231 and MCF-7 were able to form cell aggregates, with sizes and shapes of cell aggregates varying with specific microenvironmental cues: larger aggregates were observed when cells were cultured in soft hydrogels (1.8-2 kPa), a pattern observed in both static and dynamic conditions (Figs. 4 and 5). These results align with the findings of previous studies on breast cancer organoids and ovarian cancer cells, in which higher spheroid sizes were formed in lower matrix stiffness compared to higher stiffness [46,56,57]. In another study, Cavo et al. concluded that MCF-7 cells cultured in alginate based hydrogels formed smaller cell clusters (10-30 μm) when cultured in stiff hydrogels compared to larger clusters (10- 200 μm) observed in softer hydrogels [44]. These and our data suggest that hydrogels with lower stiffness have a more permissible environment for cancer cell cluster growth compared to higher stiffness hydrogels. This finds a parallel with early stages of tumour development (pre-vascularisation) that have softer matrices, allowing for cell aggregation. Soft and less dense matrices allow also a better diffusion of nutrients and oxygen; hence cell growth is promoted, and clusters increase in size (as a tumour mass *in vivo*). Shape is another parameter used to analyse cell aggregates, which informs on interactions with the surrounding environment. We have used circularity as a shape descriptor parameter to investigate cell aggregates response to different microenvironments: MDA-MB-231 cells formed low circularity aggregates in both soft and stiff hydrogels but only in the presence of high gelatin content (i.e. So-H, St-H). This effect was more pronounced in dynamic cell culture, and in the presence of mechanical forces acting on hydrogels. MCF-7 cells did not show any correlation between cell aggregates' circularity and hydrogel stiffness and gelatin content. When compared to previous studies, MDA-MB-231 cells aggregates are reported to have grape-like structure indicative of their irregular shape and mesenchymal phenotype. A study utilising PEG based hydrogels with inclusion of RGD (fibronectin-like) and GFOGER (collagen-like) peptides reported increased irregular aggregate shapes of MDA-MB-231 [46]. Additionally, this effect was reversed by blocking $\beta 1$ integrin suggesting a role of integrin mediated adhesion in this phenotype [46]. In fact, $\beta 1$ and $\beta 3$ integrins are known to be important in MDA-MB 231's adhesion to gelatin, suggesting that the observed irregularity in aggregates could be an integrin dependent phenomenon [58]. When compared to *in vivo* models, collagen deposition in breast cancers has been correlated to increased tumour grade from DCIS to IDC and invasive phenotype [20]. Our models also suggest that increasing adhesion ligand might enhance MDA-MB-231's 'motility phenotype' by increasing irregular shaped cell aggregates. We additionally observe that perfusion enhances this effect which points out to the importance of including such biophysical cues in mimicking *in vivo* phenotypes.

4.3. B-CSC dynamics

As reported by Liu et al., a heterogenous population of B-CSCs exists with subpopulations of E-CSCs ($ALDH^+$, high E-cadherin expression) and M-CSCs ($CD44^+/CD24^-$, high vimentin expression) [15]. Surprisingly, both these B-CSCs subtypes maintain their reciprocal gene expression pattern across the known molecular subtypes of breast cancer: luminal (estrogen receptor ER+, progesterone receptor PR+), Her2 enriched (Her2+), and basal/triple negative breast cancer (TNBC). However, their proportion varies across subtypes: $ALDH^+$ B-CSCs are found enriched in Her2+ cancers and slightly in luminal ones; whereas the basal subtype has majority of $CD44^+/CD24^-$ B-CSCs [15,33]. Additionally, B-CSCs have the plasticity to switch from one type to the other [15]. Hence in this study we chose a luminal subtype cell line MCF-7 (very few $ALDH^+$ cells) and TNBC cell line (high $CD44^+/CD24^-$, low $ALDH^+$) to study effects of microenvironment on B-CSC dynamics in different subtype. In a recent study, $ALDH^+$ cells from TNBC patient derived xenografts (PDX) were reported to have higher tumour initiating capacity than the $CD44^+/CD24^-$ CSCs [59]. In another study, subpopulations isolated from SUM149 showed increased invasive phenotype in $CD44^+/CD24^-$ than the $ALDH^+$ CSCs [15]. Of note in both studies, cells that were found positive for both markers (very rare population) had increased high tumour initiating capacity as well as invasive potential. While importance of heterogeneity in B-CSCs markers and phenotype has been recognised, reports are now emerging on TME's involvement in this heterogeneity. Here we observed that decreased M-CSC marker and increased E-CSC marker expression are linked with high stiffness of the encapsulating hydrogel in MDA-MB-231 cells. In contrast, in the presence of lower pH, the M-CSC population is maintained in addition to the increase in E-CSC markers with high stiffness. A similar pattern, although at a very low scale, was observed in MCF-7 cells where both $ALDH^+$ and $CD44^+/CD24^-$ cells increased in low pH and high stiffness conditions. These results suggest that higher hydrogel stiffness coupled with acidic pH (tumorigenic microenvironment) is associated with increased stem cell content consisting of both tumour initiating E-CSCs and invasive M-CSCs. Additionally, the presence of interstitial fluid flow was observed to be associated with high $CD44^+/CD24^-$ expression and low $ALDH^+$ in both cell lines, irrespective of the hydrogel stiffness. We can deduce that the reported 3D model in this study was able to recapitulate *in vivo* breast tumour observation where most $CD44^+/CD24^-$ cells were found to be located at the tumour edge (known to have high interstitial pressure and mechanical forces) whereas most $ALDH^+$ cells to be located centrally in the tumour core (known to have acidic pH) [15]. Furthermore, it confirmed that physico-chemical microenvironment can have a direct impact on B-CSCs' dynamics. PCA further confirmed clustering of B-CSCs marker expression with biophysical (stiffness, perfusion) and chemical (pH) cues in both of the cell lines. This analysis also highlighted a linear pattern (from lower stiffness to higher stiffness) in each of these clustered groups (Fig. 8C,F) suggesting involvement of mechano-transduction through matrix stiffness via a proportional response. Whilst the mechanisms through which these physico-chemical cues affect B-CSC marker expression are not yet clear, this study presents a platform that could be used to further study these interactions.

The presented results demonstrate the importance of physico-chemical cues of TME in breast cancer progression, in-line with what is reported in recent studies and with the increased number of new mechano-therapies being developed to target TME variations in addition to the selected standard of care. Examples are mechano-responsive cell system (MRCS) which use mesenchymal stem cells engineered to locally activate drugs in the presence of high stiffness tissues, and hence specifically target cancer microenvironment [60]. Further, extracellular pH equilibrium through sodium bicarbonate supplementation in mouse models was shown to increase extracellular tumoural pH and reduce metastatic load [61,62]. In view of deciphering importance of TME features, and identify more effective therapies, engineered 3D models pose as a promising next generation of non-animal technology for testing efficacy of TME targeting therapies, as well as to enhance patients' outcomes with personalized treatments.

5. Conclusions

In this study, physico-chemical cues engineered through *in vitro* modelling have shown effect on breast cancer phenotypes of cell proliferation, aggregate size and shape, and B-CSC markers. With the provision to control resolution of these cues, we were able to de-couple and understand the individual effect of each independent parameter on human breast cancer cellular phenotypes. The 3D precision models were able to capture divergent responses of the cell lines used; MCF-7's growth had decreased whereas MDA-MB 231 retained sustained growth in tumourigenic environment (stiff, dense ECM and acidic pH). On the other hand, MDA-MB 231 had increased irregularity in cell aggregates (invasive cells) with higher gelatin content (correlated to high ECM deposition *in vivo*). Additionally, we report here that the most tumourigenic conditions of stiffer, denser matrix with pH 6.5 increased proportion of both M-CSC and E-CSC subpopulations indicating increased stem cell pool in both cell lines. Precision 3D *in vitro* models can be used to delineate mechanisms involved in these phenotypes. These models represent the next generation of non-animal technologies, not only able to better recapitulate physiological microenvironments than the current *in vitro* models but also enabling better understanding of biological processes and testing of new therapeutics.

Declaration of Competing Interest

The authors declare that they have no known competing financial interests or personal relationships that could have appeared to influence the work reported in this paper.

Acknowledgements

This work was funded by PhD studentship available from President's Doctoral Scholarship from the University of Manchester and Advanced Materials in Medicine (AMM)'s Early career researcher funding. The funding source was not involved in the study design, findings or recommendations mentioned in this report. The authors thank the University of Manchester Flow Cytometry Core Facility for assistance with flow cytometry protocols. The Flow Cytometry Core Facility and BD Fortessa X-20 equipment is supported in part by the University of Manchester with assistance from Arthritis UK. The authors thank the BIOtech (University of Trento) for access and use of the field emission electron microscope, and Dr Devid Maniglio for the assistance in the acquisition of EM images. Finally, the authors would like to thank Miss Chen Zhao for her fruitful discussions on alginate hydrogels preparation.

Supplementary materials

Supplementary material associated with this article can be found, in the online version, at doi:10.1016/j.actbio.2022.08.074.

References

[1] J Winkler, A Abisoye-Ogunniyan, KJ Metcalf, Z. Werb, Concepts of extracellular matrix remodelling in tumour progression and metastasis, Nat. Commun. 11 (1) (2020) 1–19 2020 111, doi:10.1038/s41467-020-18794-x.
[2] Jonietz E. Mechanics: the forces of cancer. *Nature*2012 4917425. 2012;491(7425):S56-S57. doi:10.1038/491s56a.
[3] F Li, B Tiede, J Massagué, Y. Kang, Beyond tumorigenesis: cancer stem cells in metastasis, Cell Res. 17 (1) (2006) 3–14 2007 171, doi:10.1038/sj.cr.7310118.
[4] MA Velasco-Velázquez, VM Popov, MP Lisanti, RG. Pestell, The role of breast cancer stem cells in metastasis and therapeutic implications, Am. J. Pathol. 179 (1) (2011) 2, doi:10.1016/J.AJPATH.2011.03.005.
[5] A Pavlopoulou, Y Oktay, K Vougas, M Louka, CE Vorgias, AG. Georgakilas, Determinants of resistance to chemotherapy and ionizing radiation in breast cancer stem cells, Cancer Lett. 380 (2) (2016) 485–493, doi:10.1016/J.CANLET.2016.07.018.
[6] CE Rodríguez, DE Berardi, M Abrigo, LB Todaro, K Joffé EDB de, GL. Fiszman, Breast cancer stem cells are involved in Trastuzumab resistance through the HER2 modulation in 3D culture, J. Cell. Biochem. 119 (2) (2018) 1381–1391, doi:10.1002/JCB.26298.
[7] X Zheng, C Yu, M. Xu, Linking tumor microenvironment to plasticity of cancer stem cells: mechanisms and application in cancer therapy, Front. Oncol. 11 (2021) 2552, doi:10.3389/FONC.2021.678333/BIBTEX.
[8] EYT Lau, NPY Ho, TKW. Lee, Cancer stem cells and their microenvironment: Biology and therapeutic implications, Stem Cells Int. (2017) 2017, doi:10.1155/2017/3714190.
[9] M Al-Hajj, MS Wicha, A Benito-Hernandez, SJ Morrison, MF. Clarke, Prospective identification of tumorigenic breast cancer cells, Proc. Natl. Acad. Sci. USA 100 (7) (2003) 3983–3988, doi:10.1073/pnas.0530291100.
[10] C Chen, S Zhao, A Karnad, JW. Freeman, The biology and role of CD44 in cancer progression: therapeutic implications, J. Hematol. Oncol. 11 (1) (2018) 1–23 2018 111, doi:10.1186/S13045-018-0605-5.
[11] I Baccelli, A Schneeweiss, S Riethdorf, A Stenzinger, A Schillert, V Vogel, C Klein, M Saini, T Bäuerle, M Wallwiener, T Holland-Letz, T Höfner, M Sprick, M Scharpff, F Marmé, HP Sinn, K Pantel, W Weichert, A. Trumpp, Identification of a population of blood circulating tumor cells from breast cancer patients that initiates metastasis in a xenograft assay, Nat. Biotechnol. 31 (6) (2013) 539–544 2013 316, doi:10.1038/nbt.2576.
[12] M. Zöller, CD44: can a cancer-initiating cell profit from an abundantly expressed molecule? Nat. Rev. Cancer 11 (4) (2011) 254–267 2011 114, doi:10.1038/nrc3023.
[13] X Fang, P Zheng, J Tang, Y. Liu, CD24: from A to Z, Cell Mol. Immunol. 7 (2) (2010) 100–103 2010 72, doi:10.1038/cmi.2009.119.
[14] C Ginestier, MH Hur, E Charafe-Jauffret, F Monville, J Dutcher, M Brown, J Jacquemier, P Viens, C Kleer, S Liu, A Schott, D Hayes, D Birnbaum, MS Wicha, G Dontu, ALDH1 is a marker of normal and malignant human mammary stem cells and a predictor of poor clinical outcome, Cell Stem Cell 1 (5) (2007) 555, doi:10.1016/J.STEM.2007.08.014.
[15] S Liu, Y Cong, D Wang, Y Sun, L Deng, Y Liu, R Martin-Trevino, L Shang, SP McDermott, MD Landis, S Hong, A Adams, R D'Angelo, C Ginestier, E Charafe-Jauffret, SG Clouthier, D Birnbaum, ST Wong, M Zhan, JC Chang, MS Wicha, Breast cancer stem cells transition between epithelial and mesenchymal states reflective of their normal counterparts, Stem Cell Rep. 2 (1) (2014) 78, doi:10.1016/J.STEMCR.2013.11.009.
[16] DT Butcher, T Alliston, VM. Weaver, A tense situation: forcing tumour progression, Nat. Rev. Cancer 9 (2) (2009) 108–122, doi:10.1038/nrc2544.
[17] B Emon, J Bauer, Y Jain, B Jung, T. Saif, Biophysics of tumor microenvironment and cancer metastasis - a mini review, Comput. Struct. Biotechnol. J. 16 (2018) 279–287, doi:10.1016/J.CSBJ.2018.07.003.
[18] P Lu, VM Weaver, Z. Werb, The extracellular matrix: a dynamic niche in cancer progression, J. Cell Biol. 196 (4) (2012) 395–406, doi:10.1083/jcb.201102147.
[19] A Samani, J Zubovits, D. Plewes, Elastic moduli of normal and pathological human breast tissues: an inversion-technique-based investigation of 169 samples, Phys. Med. Biol. 52 (6) (2007) 1565–1576, doi:10.1088/0031-9155/52/6/002.
[20] I Acerbi, L Cassereau, I Dean, Q Shi, A Au, C Park, YY Chen, J Liphardt, ES Hwang, VM. Weaver, Human breast cancer invasion and aggression correlates with ECM stiffening and immune cell infiltration, Integr. Biol. 7 (10) (2015) 1120–1134, doi:10.1039/C5IB00040H.
[21] RA Gatenby, ET Gawlinski, AF Gmitro, B Kaylor, RJ. Gillies, Acid-mediated tumor invasion: a multidisciplinary study, Cancer Res. 66 (10) (2006) 5216–5223, doi:10.1158/0008-5472.CAN-05-4193.
[22] M Chen, C Chen, Z Shen, X Zhang, Y Chen, F Lin, X Ma, C Zhuang, Y Mao, H Gan, P Chen, X Zong, R. Wu, Extracellular pH is a biomarker enabling detection of breast cancer and liver cancer using CEST MRI, Oncotarget 8 (28) (2017) 45759, doi:10.18632/ONCOTARGET.17404.
[23] V Estrella, T Chen, M Lloyd, J Wojtkowiak, HH Cornnell, A Ibrahim-Hashim, K Bailey, Y Balagurunathan, JM Rothberg, BF Sloane, J Johnson, RA GR Gatenby, Acidity generated by the tumor microenvironment drives local invasion, Cancer Res. 73 (5) (2013) 1524–1535, doi:10.1158/0008-5472.CAN-12-2796.

[24] Q Shi, X Le, B Wang, JL Abbruzzese, Q Xiong, Y XK He, Regulation of vascular endothelial growth factor expression by acidosis in human cancer cells, Oncogene 20 (28) (2001), doi:10.1038/SJ.ONC.1204500.
[25] ZE Walton, CH Patel, RC Brooks, Y Yu, A Ibrahim-Hashim, M Riddle, A Porcu, T Jiang, BL Ecker, F Tameire, C Koumenis, AT Weeraratna, DK Welsh, R Gillies, JC Alwine, L Zhang, JD DC Powell, Acid suspends the circadian clock in hypoxia through inhibition of mTOR, Cell 174 (1) (2018) 72-87.e32, doi:10.1016/J.CELL.2018.05.009.
[26] M Wagner, H. Wiig, Tumor interstitial fluid formation, characterization, and clinical implications, Front. Oncol. 5 (MAY) (2015) 115, doi:10.3389/FONC.2015.00115/BIBTEX.
[27] JM Munson, AC. Shieh, Interstitial fluid flow in cancer: implications for disease progression and treatment, Cancer Manag. Res. 6 (2014) 317, doi:10.2147/CMAR.S65444.
[28] MA Swartz, ME. Fleury, Interstitial flow and its effects in soft tissues, Annu. Rev. Biomed. Eng. 9 (1) (2007) 229–256, doi:10.1146/annurev.bioeng.9.060906.151850.
[29] Polacheck WJ, Charest JL, Kamm RD, Chien S. Interstitial flow influences direction of tumor cell migration through competing mechanisms. doi:10.1073/pnas.1103581108.
[30] U Haessler, JCM Teo, D Foretay, P Renaud, MA. Swartz, Migration dynamics of breast cancer cells in a tunable 3D interstitial flow chamber, Integr. Biol. 4 (4) (2012) 401–409, doi:10.1039/c1ib00128k.
[31] W Asghar, R El Assal, H Shafiee, S Pitteri, R Paulmurugan, U. Demirci, Engineering cancer microenvironments for in vitro 3-D tumor models, Mater. Today 18 (10) (2015) 539–553, doi:10.1016/J.MATTOD.2015.05.002.
[32] SA. Langhans, Three-dimensional in vitro cell culture models in drug discovery and drug repositioning, Front. Pharmacol. 9 (JAN) (2018) 6, doi:10.3389/fphar.2018.00006.
[33] MD Brooks, ML Burness, MS. Wicha, Therapeutic implications of cellular heterogeneity and plasticity in breast cancer, Cell Stem Cell 17 (3) (2015) 260–271, doi:10.1016/J.STEM.2015.08.014.
[34] A Tirella, G AA Mattei, Strain rate viscoelastic analysis of soft and highly hydrated biomaterials, J. Biomed. Mater. Res. A 102 (10) (2014) 3352–3360, doi:10.1002/JBM.A.34914.
[35] A Tirella, G Mattei, M La Marca, A Ahluwalia, N Tirelli, Functionalized enzyme-responsive biomaterials to model tissue stiffening in vitro, Front. Bioeng. Biotechnol. 0 (2020) 208, doi:10.3389/FBIOE.2020.00208.
[36] B Almari, D Brough, M Harte, A. Tirella, Fabrication of amyloid-β-secreting alginate microbeads for use in modelling Alzheimer's disease, J. Vis. Exp. 2019 (149) (2019), doi:10.3791/59597.
[37] T Azimi, M Loizidou, MV. Dwek, Cancer cells grown in 3D under fluid flow exhibit an aggressive phenotype and reduced responsiveness to the anticancer treatment doxorubicin, Sci. Rep. 10 (1) (2020) 12020, doi:10.1038/s41598-020-68999-9.
[38] D Mazzei, MA Guzzardi, S Giusti, A. Ahluwalia, A low shear stress modular bioreactor for connected cell culture under high flow rates, Biotechnol. Bioeng. 106 (1) (2010) 127–137, doi:10.1002/BIT.22671.
[39] G Xiang, E Lippens, S Hafeez, GN Duda, S Geissler, TH. Qazi, Oxidized alginate beads for tunable release of osteogenically potent mesenchymal stromal cells, Mater. Sci. Eng. C 104 (2019) 109911, doi:10.1016/J.MSEC.2019.109911.
[40] B Sarker, T Zehnder, SN Rath, RE Horch, U Kneser, R Detsch, AR. Boccaccini, Oxidized alginate-gelatin hydrogel: a favorable matrix for growth and osteogenic differentiation of adipose-derived stem cells in 3D, ACS Biomater. Sci. Eng. 3 (8) (2017) 1730–1737, doi:10.1021/acsbiomaterials.7b00188.
[41] A Negro, T Cherbuin, MP. Lutolf, 3D inkjet printing of complex, cell-laden hydrogel structures, Sci. Rep. 8 (1) (2018) 1–9, doi:10.1038/s41598-018-35504-2.
[42] Zhang B, Shan DH, Li D, Li Z ran, Zhu K shun, Jiang Z. bo, Huang M sheng. Different methods of detaching adherent cells significantly affect the detection of TRAIL receptors. doi:10.1177/030089161209800619.
[43] Rosa JMR de la, Wubetu J, N Tirelli, A Tirella, Colorectal tumor 3D in vitro models: advantages of biofabrication for the recapitulation of early stages of tumour development, Biomed. Phys. Eng. Express 4 (4) (2018) 045010, doi:10.1088/2057-1976/AAC1C9.
[44] M Cavo, M Fato, L Peñuela, F Beltrame, R Raiteri, S. Scaglione, Microenvironment complexity and matrix stiffness regulate breast cancer cell activity in a 3D in vitro model, Sci. Rep. 6 (1) (2016) 1–13, doi:10.1038/srep35367.
[45] E Lhuissier, C Bazille, J Aury-Landas, N Girard, J Pontin, M Boittin, K Boumediene, C. Baugé, Identification of an easy to use 3D culture model to investigate invasion and anticancer drug response in chondrosarcomas, BMC Cancer 17 (1) (2017) 1–12, doi:10.1186/S12885-017-3478-Z/TABLES/2.
[46] LA Sawicki, EM Ovadia, L Pradhan, JE Cowart, KE Ross, CH Wu, AM. Kloxin, Tunable synthetic extracellular matrices to investigate breast cancer response to biophysical and biochemical cues, APL Bioeng. 3 (1) (2019) 016101, doi:10.1063/1.5064596.
[47] D Huh, BD Matthews, A Mammoto, M Montoya-Zavala, H Yuan Hsin, DE Ingber, Reconstituting organ-level lung functions on a chip, Science (80-) 328 (5986) (2010) 1662–1668, doi:10.1126/science.1188302.
[48] BX Ho, NMQ Pek, BS. Soh, Disease modeling using 3D organoids derived from human induced pluripotent stem cells, Int. J. Mol. Sci. 19 (4) (2018) 936 *2018, Vol 19, Page 936*, doi:10.3390/IJMS19040936.
[49] LE Barney, EC Dandley, LE Jansen, NG Reich, AM Mercurio, SR. Peyton, A cell-ECM screening method to predict breast cancer metastasis †, Integr. Biol. 7 (2015) 198, doi:10.1039/c4ib00218k.
[50] S S. Franco, K Szczesna, MS Iliou, M Al-Qahtani, A Mobasheri, J Kobolák, A Dinnyés, In vitro models of cancer stem cells and clinical applications, BMC Cancer 16 (2) (2016) 23–49 2016 162, doi:10.1186/S12885-016-2774-3.
[51] KY Lee, DJ. Mooney, Alginate: properties and biomedical applications, Prog. Polym. Sci. 37 (1) (2012) 106–126, doi:10.1016/j.progpolymsci.2011.06.003.
[52] SO Sarrigiannidis, JM Rey, O Dobre, C González-García, MJ Dalby, M. Salmeron-Sanchez, A tough act to follow: collagen hydrogel modifications to improve mechanical and growth factor loading capabilities, Mater. Today Bio. 10 (2021) 100098, doi:10.1016/J.MTBIO.2021.100098.
[53] EA Aisenbrey, WL. Murphy, Synthetic alternatives to Matrigel, Nat. Rev. Mater. 5 (7) (2020) 539, doi:10.1038/S41578-020-0199-8.
[54] SR Caliari, JA. Burdick, A practical guide to hydrogels for cell culture, Nat. Methods 13 (5) (2016) 405–414, doi:10.1038/nmeth.3839.
[55] AR Freischel, M Damaghi, JJ Cunningham, A Ibrahim-Hashim, RJ Gillies, RA Gatenby, JS. Brown, Frequency-dependent interactions determine outcome of competition between two breast cancer cell lines, Sci. Rep. 11 (1) (2021) 1–18, doi:10.1038/s41598-021-84406-3.
[56] D Loessner, KS Stok, MP Lutolf, DW Hutmacher, JA Clements, SC. Rizzi, Bioengineered 3D platform to explore cell–ECM interactions and drug resistance of epithelial ovarian cancer cells, Biomaterials 31 (32) (2010) 8494–8506, doi:10.1016/J.BIOMATERIALS.2010.07.064.
[57] JN Beck, A Singh, AR Rothenberg, JH Elisseeff, AJ. Ewald, The independent roles of mechanical, structural and adhesion characteristics of 3D hydrogels on the regulation of cancer invasion and dissemination, Biomaterials 34 (37) (2013) 9486–9495, doi:10.1016/J.BIOMATERIALS.2013.08.077.
[58] BT Beaty, VP Sharma, JJ Bravo-Cordero, MA Simpson, RJ Eddy, AJ Koleske, J. Condeelis, β1 integrin regulates Arg to promote invadopodial maturation and matrix degradation, Mol. Biol. Cell 24 (11) (2013) 1661–1675, doi:10.1091/MBC.E12-12-0908/ASSET/IMAGES/LARGE/1661FIG7.JPEG.
[59] M Liu, Y Liu, L Deng, D Wang, X He, L Zhou, MS Wicha, F Bai, S. Liu, Transcriptional profiles of different states of cancer stem cells in triple-negative breast cancer, Mol. Cancer 17 (1) (2018), doi:10.1186/S12943-018-0809-X.
[60] SX Zhang, L Liu, W. Zhao, Targeting biophysical cues: a niche approach to study, diagnose, and treat cancer, Trends Cancer 4 (4) (2018) 268–271, doi:10.1016/J.TRECAN.2018.02.006.
[61] MF McCarty, J. Whitaker, Manipulating tumor acidification as a cancer treatment strategy, Altern. Med. Rev. 15 (3) (2010) 264–272.
[62] IF Robey, BK Baggett, ND Kirkpatrick, DJ Roe, J Dosescu, BF Sloane, AI Hashim, DL Morse, N Raghunand, RA GR Gatenby, Bicarbonate increases tumor pH and inhibits spontaneous metastases, Cancer Res. 69 (6) (2009) 2260–2268, doi:10.1158/0008-5472.CAN-07-5575.